



HAL
open science

East Asian monsoon and westerly jet driven changes in climate and surface conditions in the NE drylands of China since the Late Pleistocene

Steve Pratte, Kushan Bao, Chuxian Li, Wenfang Zhang, Gaël Le Roux, Gaojun Li, François de Vleeschouwer

► To cite this version:

Steve Pratte, Kushan Bao, Chuxian Li, Wenfang Zhang, Gaël Le Roux, et al.. East Asian monsoon and westerly jet driven changes in climate and surface conditions in the NE drylands of China since the Late Pleistocene. *Quaternary Science Reviews*, 2024, 331, pp.108637. 10.1016/j.quascirev.2024.108637 . hal-04708283

HAL Id: hal-04708283

<https://hal.science/hal-04708283v1>

Submitted on 11 Oct 2024

HAL is a multi-disciplinary open access archive for the deposit and dissemination of scientific research documents, whether they are published or not. The documents may come from teaching and research institutions in France or abroad, or from public or private research centers.

L'archive ouverte pluridisciplinaire **HAL**, est destinée au dépôt et à la diffusion de documents scientifiques de niveau recherche, publiés ou non, émanant des établissements d'enseignement et de recherche français ou étrangers, des laboratoires publics ou privés.

1 **East Asian monsoon and Westerly Jet driven changes in climate and surface**
2 **conditions in the NE drylands of China since the Late Pleistocene**

3 Steve Pratte^{1,3}, Kushan Bao^{2,3}, Chuxian Li⁴, Wenfang Zhang³, Gaël Le Roux⁵, Gaojun Li⁶, and
4 François De Vleeschouwer⁷

5 ¹ School of Earth Sciences, Zhejiang University, Hangzhou, China

6 ² School of Geography, South China Normal University, Guangzhou 510631, China

7 ³ State Key Laboratory of Lake Science and Environment, Nanjing Institute of Geography and
8 Limnology, Chinese Academy of Sciences, Nanjing, China

9 ⁴ Institute of Geography and Oeschger Center for Climate Change Research, University of Bern,
10 3012 Bern, Switzerland

11 ⁵ Laboratoire écologie fonctionnelle et environnement, Université de Toulouse, CNRS, INPT,
12 UPS, Toulouse, France

13 ⁶ Key Laboratory of Surficial Geochemistry, Department of Earth and Planetary Sciences,
14 Nanjing University, Nanjing, China

15 ⁷ Instituto Franco-Argentino para el Estudio del Clima y sus Impactos (UMI IFAECI/CNRS-
16 CONICET-UBA-IRD), University of Buenos Aires, Buenos Aires, Argentina

17

18 Corresponding author: Kunshan Bao (ksbao@scnu.edu.cn)

19

20

21

22

23

24

25

26

27

28

29

30

31

32 **Abstract**

33 The East Asian summer monsoon (EASM) is a major component of the global climate yet, the
34 causes for the past spatiotemporal variability of EASM rainfall, its interactions and impacts remain
35 unresolved. Here we use the Sr-Nd isotopes and rare earth elements composition of dust in a peat
36 record from northeast (NE) China to investigate the relationship between the East Asian monsoon
37 and Westerly Jet (WJ) over East Asia since the Late Pleistocene (14 cal ka BP). The NE drylands
38 of China dominate the dust fraction (Hunshandake, Horqin; 44-88%) with a contribution from the
39 deserts of NW China (Badain Jaran, Tengger, Taklamakan; 10-44%), suggesting an influence of
40 the WJ. Dust deposition varied during the Holocene, displaying a minimum between 8.0-6.0 cal
41 ka BP and two peaks at 5.8-3.8 and 1.7-0.3 cal ka BP. Changes in dust flux are opposite to the East
42 Asian winter monsoon intensity profile, suggesting a limited influence of the winter monsoon. The
43 EASM appears to have played a more significant role in the dust cycle, with increasing dust fluxes
44 corresponding with lower EASM precipitation. Variations in dust flux from NE drylands display
45 shifts reflecting changes in EASM precipitations and dune activity along the EASM margin, where
46 the dust originates from. To account for the influence of the WJ, we propose that the meridional
47 position and intensity of the WJ also affected dust emission in the drylands' region. A more
48 northward position of the WJ allows the EASM front further north, generating more precipitations
49 over the NE drylands, reducing the extent of arid areas, and resulting in less dust emission from
50 dune activity, while the opposite occurs with a strong, more southerly WJ. Anthropogenic
51 activities are likely to have had an increasing impact on the dust cycle over the late Holocene.
52 Nevertheless, the presence of inconsistencies in records, coupled with a simultaneous decline in
53 climatic conditions (mainly precipitations) during the same timeframe, hinders the precise
54 assessment of the influence of human activities on dust emissions in the region.

55

56 **1. Introduction**

57 The East Asian summer monsoon (EASM) has a major influence on global climate (An, 2000),
58 controlling most aspects of hydrology in East Asia. Its extent, intensity, and associated
59 precipitations display clear variations during the Holocene (Chen et al., 2015; Goldsmith et al.,
60 2017) and have a considerable influence on the economy and lives of billions of people.
61 Understanding its past variability, interactions, and impacts is important to determine its future
62 response to climate change. The spatiotemporal heterogeneity in the Holocene maximum in
63 monsoonal rainfall in northern China has long been a matter of debate, which prevents a complete
64 understanding of the EASM behaviour and dynamics (An, 2000; Chen et al., 2015; Herzschuh et
65 al., 2019; Li et al., 2020a; Zhou et al., 2016). Recently, evidence has pointed to interactions
66 between the EASM and the northward position and orientation of the Westerly Jet (WJ) stream as
67 an explanation for the spatiotemporal variations in EASM precipitations (Chiang et al., 2015;
68 Herzschuh et al., 2019; Li et al., 2020b), and also for changes in the East Asian winter Monsoon
69 (EAWM) (Nagashima et al., 2007). The position of the WJ has varied during the Holocene and
70 has been found to affect EASM precipitations and temperature, conditions often being drier and
71 colder in northern China when the WJ was further south and the opposite when it was in a
72 northward position (Bae et al., 2020; Nagashima et al., 2013; Wang et al., 2020). Hence,

73 reconstructing paleo-synoptic conditions remains critical in the understanding of East Asian
74 climate dynamics and its impacts on Earth's surface processes.

75 Mineral dust acts both as a driver and a recorder of climate changes, its emission, transport, and
76 deposition being a function of a series of climatic and environmental factors, such as aridity, air
77 mass trajectories, and human activities (Marx et al., 2018). Paleo-dust records produce clear
78 evidence of the variability of dust deposition in response to climate changes and provide multi-
79 proxy data on changes in aridity, synoptic systems, and wind strength (Kohfeld and Harrison, 2001;
80 Marx et al., 2018; Nagashima et al., 2007) as well as anthropogenic activities. East Asia contains
81 some of the world's largest dust sources, accounting for about a quarter of global dust emissions
82 (Ginoux et al., 2004). The East Asian monsoon (EAM) and WJ affect East Asian climate variability,
83 induce changes in surface conditions in source regions and have considerable effects on dust
84 emission (Sun et al., 2001). Changes in dust levels also have important societal and environmental
85 impacts (Goudie, 2009), e.g., Asian dust affects the biogeochemical cycle of P and Fe in the North
86 Pacific (Letelier et al., 2019). Therefore, paleo-dust records downwind of source regions are
87 important to better constrain the variability of the East Asian climate, but also the impacts of
88 synoptic systems on atmospheric dust loadings.

89 Rare earth elements (REE) display very similar chemical properties and inherit their chemical
90 composition from their source material. It is generally accepted that REE are not significantly
91 affected by crustal weathering (McLennan, 1989; Nesbitt, 1979) and hence both their elemental
92 and isotopic (Nd often combined with Sr or Pb) composition have been used to trace sediment
93 provenance (Biscaye et al., 1997; Chen et al., 2007a; Ferrat et al., 2011; Gaiero et al., 2004; Gallet
94 et al., 1998; McLennan, 1989). In East Asia, these paleo-provenance proxies have been used to
95 characterize the deserts and dune fields of northern China (Chen et al., 2007a; Ferrat et al., 2011;
96 Hu and Yang, 2016; Jiang and Yang, 2019; Nakano et al., 2004; Rao et al., 2008; Rao et al., 2011;
97 Xie and Chi, 2016; Xie et al., 2020; Yang et al., 2009). The seminal work by Chen et al. (2007a)
98 has shown that based on Sr-Nd isotopic compositions of specific size fractions ($<75\mu\text{m}$ and <5
99 μm), the drylands of East Asia can be divided into three distinct regions owing to the source
100 material from which they are derived (Fig. 1). These characteristic units have since been used
101 extensively to trace the specific sources of dust in environmental archives and to reconstruct their
102 related changes in the synoptic systems in Asia (Beaudon et al., 2022; Chen and Li, 2013; Ferrat
103 et al., 2012; Miyazaki et al., 2016; Xie et al., 2019; Zhang et al., 2018a; Zhao et al., 2015).

104 Northeastern (NE) China, located downwind of the major dust sources of East Asia, is under the
105 influence of both the EAM system and the WJ (Fig. 1). While dust records in peat from NE China
106 show that dust is coming from the Chinese drylands (Fig. 1) (Pratte et al., 2020), the exact drylands
107 are yet to be determined. In this study, we aim to utilize geochemical and isotopic signatures of
108 the mineral fraction (i.e. dust component) in peat to constrain the dust source(s) to Hani peatland
109 in NE China and identify associated climatic drivers (Fig. 1). In achieving this, we investigate the
110 REE compositions and Sr-Nd isotopic signatures of peat in comparison to those of potential east
111 Asian sources in the literature and from local sources collected near the study site. We further
112 identify how the dominant atmospheric systems in East Asia (i.e. WJ and EAM) affected
113 environmental changes in the dust source regions since the Late Pleistocene.

114

115 2. Materials and Methods

116 2.1 Study area and core collection

117 The Hani peatland (42°13'27.0''N; 126°31'110.0''E; 900 m.a.s.l.; 18 km²) is located in the Jilin
118 Province, NE China (Fig. 1A). The area is dominated by Quaternary volcanic deposits (alkali
119 basalts, tholeiitic basalts, trachyte and pyroclastic deposits) forming the Longgang volcanic field
120 (LGVF), which overlays the Upper Archean Anshan migmatite group, part of the North China
121 craton and composed of migmatite, gneiss, amphibolite and quartzite (*Bureau of Geology and*
122 *Mineral Ressources of Jilin Province, 1988*). The climate in the study area is governed by the East
123 Asian monsoon and is characterized by a strong seasonality, with warm/moist conditions through
124 the influence of air masses from the Pacific during the summer and cold/dry air masses from the
125 Asian continent during winter (Schettler et al., 2006a). The EAWM and westerly winds strongly
126 affect the region during winter and especially spring, when conditions are favourable for the
127 occurrence of dust storms in spring (Chu et al., 2009). The study site is located in a region that was
128 devoid of significant human activities that would have influenced local dust emission prior to the
129 18th century (Makohonienko et al., 2008). As such, Hani peatland is an ideal record to study
130 regional to large-scale dust transport.

131 Peat core collection, processing for physical characteristics and chronological control are detailed
132 in Pratte et al. (2020). Briefly, a 10m profile, of which 9.3m is composed of peat (Hani-3), was
133 collected from the Hani peatland. The core, dated by ¹⁴C AMS (15 dates), shows that peat
134 accumulation initiated around 14.5 cal ka BP (Fig. 1C). The representativity of the Hani peat record
135 as a geochemical archive of aeolian dust as already been established (Pratte et al., 2020). Surface
136 samples from potential local sources (soils, scoria, rocks) were collected near the study site to
137 characterize the isotopic composition of local dust sources (Fig. 1B). The surface soils were
138 separated as bulk and <63µm fractions, dried and ground while consolidated samples, e.g. basalt
139 and scoria, were cut, ground and analyzed as bulk materials.

140

141 2.2 Sr-Nd isotopes analyses

142 Details on peat sub-sampling and sample preparation are described in Pratte et al. (2020).
143 Homogenized and ashed (550°C for 6h) peat samples were processed and digested in an acid
144 mixture (HNO₃-HF) following an established protocol (Zhang et al., 2016). The siliciclastic Sr-Nd
145 isotopic ratios of 46 peat samples, one scoria, one rock and three soil samples (bulk and <63µm)
146 were determined by multi-collector ICP-MS at Nanjing University after elution through a series
147 of anionic resins. Replicate analyses of the SRM987 (⁸⁷Sr/⁸⁶Sr = 0.71034±0.00026) and
148 JMCNd₂O₃ (Nd oxide) certified reference materials (CRM) yielded values of 0.710268±13 (n=9)
149 and 0.512093±7 (n=7) respectively. The chemical procedure was verified using the BCR-2 CRM
150 (⁸⁷Sr/⁸⁶Sr = 0.705000±11; ¹⁴³Nd/¹⁴⁴Nd = 0.512637±13) showing values of 0.705029±0.9 (n=2) and
151 0.512627±6 (n=2) for ⁸⁷Sr/⁸⁶Sr and ¹⁴³Nd/¹⁴⁴Nd respectively. The Nd isotopic composition of 29
152 additional samples was determined by TIMS at *Observatoire Midi-Pyrénées* in Toulouse following

153 Vanneste et al. (2015). Instrumental drift was monitored using Nd reference material La Jolla
 154 ($^{143}\text{Nd}/^{144}\text{Nd} = 0.511858$) for which values of 0.511843 ± 11 (n=11) were obtained. Procedural
 155 blanks for Nd are negligible, while replicate samples between the two measurement methods were
 156 generally within the $^{143}\text{Nd}/^{144}\text{Nd}$ values error bars. The $^{87}\text{Sr}/^{86}\text{Sr}$ of the Hani samples was corrected
 157 for the proportion of $<2\mu\text{m}$ particles (see section 2.4). Rare earth element and Sr concentrations
 158 were previously measured (Pratte et al., 2020) on dry powdered peat (~100 mg) using Q-ICP-MS
 159 and are used as a support for Sr-Nd data and to reconstruct the dust flux (see Fig. 2, Table S1).
 160 The most probable sources for the dust were identified and used as end members (Fig. S2) to
 161 estimate their respective contributions based on the hyperbolic mixing relationship of ratio-ratio
 162 plots (section 2.3).

163 Epsilon neodymium (ϵNd) was calculated according to DePaolo and Wasserburg (1976):

164 (1)
$$\epsilon\text{Nd} = \left(\frac{\left(\frac{^{143}\text{Nd}}{^{144}\text{Nd}} \right)}{0.512638} - 1 \right) \times 10000$$

165 where 0.512638 corresponds to the chondritic uniform reservoir (CHUR) and represents present-
 166 day average Earth value (Jacobsen and Wasserburg, 1980).

167

168 2.3 End member calculation and source related dust flux

169 Comparing the Sr-Nd isotopic composition and REE ratios of the Hani peat samples with those of
 170 the potential source areas in northern China (Fig. 1A), the most probable sources for the mineral
 171 dust were identified and used as end members (median values; Fig. S2) to estimate their respective
 172 contribution. The contribution of each source end-member was calculated based on the hyperbolic
 173 mixing relationship of ratio-ratio plots as described in Albarède (1995):

174 (2)
$$\left(\frac{C^{i2}}{C^{i1}} \right)_{mix} = \frac{\sum_{j=1}^n C_j^{i2} f_j}{C_{mix}^{i1}}$$

175 Where C^{i1} and C^{i2} are the Nd and Sr isotopes or REE concentrations in a mixture of n end-
 176 members j , while f represents the fraction of end-member j in the mineral fraction recovered in
 177 samples of Hani peatland. The most probable source proportions were determined using the root
 178 mean square error (RMSE), where a value close to zero correspond to a closer fit to the measured
 179 value (Table S3). This approach was successfully applied to trace the source of aeolian dust
 180 deposited to a peatland from Amsterdam Island in the Indian Ocean (Li et al., 2020).

181 The dust accumulation rate, i.e. dust flux ($\text{g m}^{-2} \text{a}^{-1}$) was calculated using the sum of REE following
 182 the formula:

183 (3)
$$\text{Dust flux}_i = \frac{\sum[\text{REE}]_i \times \text{PAR}_i \times \sigma_i}{\sum[\text{REE}]_{\text{UCC}}} \times 10000$$

184 where $\sum[\text{REE}]_i$ is the sum of REE concentrations in a specific sample i , $\sum[\text{REE}]_{\text{UCC}}$ is the sum of
 185 REE concentrations in the upper continental crust ($143 \mu\text{g g}^{-1}$; (Wedepohl, 1995)), PAR is the peat
 186 accumulation rate (cm a^{-1}) calculated based on the age-depth model and σ is the bulk density of

187 the sample (g cm^{-3}). Afterward, the relative proportion of dust contribution from specific sources
188 (Fig. 5 and S3) were used to estimate their specific dust deposition flux (ex.: dust flux from NE
189 drylands in Fig. 6 and 7).

190 The resulting source-specific dust fluxes were submitted to change point analysis to identify
191 significant shifts in the dust record. The change point analysis was performed using the Change-
192 point Analyzer 2.0 software (Taylor Enterprise). The method combines cumulative sum charts
193 (difference between the values and the average) and bootstrapping to detect changes (Taylor, 2000).
194 Ten thousand bootstraps were performed and only changes with probabilities greater than 99%
195 were considered.

196

197 *2.4 $^{87}\text{Sr}/^{86}\text{Sr}$ as a dust proxy in peat and potential grain size effect on $^{87}\text{Sr}/^{86}\text{Sr}$ values*

198 Sr is known to be affected by mineral dissolution and diffusion in peat (Shotyk, 1997; Steinmann
199 and Shotyk, 1997), which can affect its reliability as a proxy of dust deposition and provenance.
200 Sr concentrations in Hani-3 profile are generally low with an average of $21 \pm 6 \mu\text{g g}^{-1}$ above 635
201 cm of depth (excluding the peak around 180 cm) for $41 \pm 12 \mu\text{g g}^{-1}$ below (Fig. 2), a difference
202 much lower than those observed in records affected by Sr remobilization (Pratte et al., 2017;
203 Steinmann and Shotyk, 1997). This suggests that mineral dissolution and Sr remobilization is
204 limited in the Hani-3 core and that it can be used as a dust archive. Furthermore, after removing
205 the potentially labile fraction of Sr through a weak acid treatment, the trends in the $^{87}\text{Sr}/^{86}\text{Sr}$ signal
206 closely follow those of the ϵNd (Fig. 2), which confirms that the labile fraction was removed and
207 that the $^{87}\text{Sr}/^{86}\text{Sr}$ represents the siliciclastic fraction and can be used to reconstruct changes in dust
208 source(s).

209 The grain size of the Hani samples is generally dominated by silts with a median grain size of 10-
210 $18.7 \mu\text{m}$ and more than 95% in the $<75 \mu\text{m}$ fraction (Fig. S1; (Pratte et al., 2020)), which makes
211 them comparable with the potential sources in the literature. The loess deposits of NE China
212 display lower $^{87}\text{Sr}/^{86}\text{Sr}$ values than most Hani samples, but very similar ϵNd (Fig. 3). The influence
213 of grain size sorting on Sr isotopic ratios is well documented, with higher ratios being reported in
214 finer fractions ($<2 \mu\text{m}$ and $<5 \mu\text{m}$) (Biscaye et al., 1997; Chen et al., 2007a; Feng et al., 2009;
215 Grousset et al., 1992; Meyer et al., 2011). This is supported by the fact that the loess grain size is
216 generally coarser than that of the Hani samples. This can likely be explained by the Hani peatland
217 location, i.e. at further distances from the NE drylands than the loess deposit and in a mountain
218 range, the Changbai Mountains, that likely partially intercept coarser particles. Given the low
219 amounts of samples available, it was not possible to separate the $<2 \mu\text{m}$ fraction of the mineral
220 matter in Hani and analyse it separately for $^{87}\text{Sr}/^{86}\text{Sr}$. Instead we elected to make a correction to
221 the $^{87}\text{Sr}/^{86}\text{Sr}$ values of the bulk samples based on the proportion of $<2 \mu\text{m}$ particle in each sample
222 analysed (Fig. S3). The clay particles ($<2 \mu\text{m}$) of the Chinese drylands have $^{87}\text{Sr}/^{86}\text{Sr}$ ratios 0.006
223 higher on average than the other grain size fraction (Chen et al., 2007a). The $<2 \mu\text{m}$ fraction in
224 Hani samples range between 6 and 17%, which corresponds to an estimated maximum increase of
225 0.001 in the $^{87}\text{Sr}/^{86}\text{Sr}$ ratios of the Hani samples.

226

227 3. Results

228 3.1 Summary of the core general characteristics

229 A detailed description of the physical characteristics of the core is given in Pratte et al. (2020) and
230 a summary of the key data is presented in Fig. 2. The peat is generally dominated by sedges with
231 *Sphagnum* spp. present in various proportions down to 931 cm of depth. Lithological changes in
232 the peat core correspond mainly to variations in decomposition state and color along with the
233 presence of noticeable mineral-rich layers at 1.7-1.8, 10.6-10.7, 11.2-11.4 and 11.9-12.0 cal ka BP
234 (Fig. S1). The ash content of the peat ranges between 5-58% with an average of $21\pm 4\%$ during the
235 Holocene, when excluding the mineral-rich layers, which is lower and more stable than the older
236 part (>11.5 cal ka BP) of the core ($30\pm 8\%$). The particle grain size of the mineral fraction of peat
237 is usually dominated by a mode in the fine-silt fraction, but still displays a similar pattern as ash
238 content, i.e. samples with greater median grain size are more frequent in the lower part of the core
239 and in the mineral-rich layers.

240

241 3.2 Geochemical composition of the peat

242 Isotopic compositions of $^{87}\text{Sr}/^{86}\text{Sr}$ and ϵNd samples from Hani and local sources are shown in Fig.
243 3 and Table S2. The ϵNd of the peat samples ranges between -0.5 and -9.8, while the $^{87}\text{Sr}/^{86}\text{Sr}$
244 varies from 0.704687 to 0.715998 (Fig. 3 and Table S3). The ϵNd of the scoria and rocks is +1.1
245 and +1.7, while $^{87}\text{Sr}/^{86}\text{Sr}$ values are 0.704555 and 0.704418 (Fig. 3). The isotopic composition of
246 the soils ranges between that of the scoria and volcanic rocks and of the Hani peat samples with
247 values of +0.7 to -4.8 and 0.704618 to 0.707578 for ϵNd and $^{87}\text{Sr}/^{86}\text{Sr}$ respectively (Fig. 3).

248 REE patterns of the Hani peat samples, local sources (soils, scoria, volcanic deposits), and the <5
249 μm and $<75 \mu\text{m}$ fractions from potential Chinese dust sources (deserts and dune fields; Fig. 1) are
250 shown in Fig. 4A-B. The greater part of the Hani samples displays relatively flat REE patterns
251 with a slight enrichment in middle REE (Fig. 4B). These samples are also characterized by near-
252 neutral Eu anomalies ($\text{Eu}/\text{Eu}^*_\text{N} = 0.94-1.07$). In comparison, a number of peat samples ($n=19$) also
253 have a relatively flat REE pattern, but display a clear positive Eu anomaly ($\text{Eu}/\text{Eu}^*_\text{N} > 1.10$) while
254 three samples show lower light REE contents (Fig. 4C, red curves). Soils, scoria, and rock samples
255 measured in this study and from the literature also display positive $\text{Eu}/\text{Eu}^*_\text{N}$ anomalies ranging
256 between 1.20 and 1.98 (Fig. 4C).

257

258 4. Discussion

259 4.1 Dust provenance

260 The comparison of the REE patterns of the Hani samples with those of potential sources confirms
261 the mainly allochthonous origin of the dust (Pratte et al., 2020). Most of the Hani samples show a
262 close resemblance to the patterns of the drylands and loess of northern China with a slight middle
263 REE enrichment (Fig. 4A and B). However, the similarity of the REE patterns of the various

264 deserts and dune fields does not allow for the identification of the precise source on this basis. The
265 presence of a positive Eu/Eu* anomaly in a number of samples (n=19) shows that local sources
266 contribute significantly during specific events (Fig. 4C). In addition, samples with higher Eu/Eu*
267 anomalies, especially those around 1.7 cal ka BP, generally contain more plagioclase feldspars
268 (Pratte et al., 2020), known to display positive Eu anomalies (Wilson, 2000). Hence, the REE
269 composition of the Hani sample allow the distinction between the local mafic source(s) from the
270 allochthonous source(s) from the deserts and drylands of China.

271 As Chinese drylands were identified as the main source of mineral material in Hani peatland (Pratte
272 et al., 2020), we use Sr-Nd isotopes, in conjunction with potential source areas, to narrow down
273 the most likely drylands. These drylands are divided into three isotopic regions (Fig. 1a): 1) the
274 drylands along the northern boundary of China (NBC: Hunshandake, Horqin, Hulun Buir, Songnen
275 and Gurbantungut); 2) the deserts along the northern margin of the Tibetan Plateau (NMTP:
276 Taklamakan, Qaidam, Badain Jaran and Tengger), and 3) the deserts on or near the Ordos Plateau
277 (Hobq and Mu Us) (Chen et al., 2007a). Most peat samples are within the fields of the NE drylands
278 (NED; Hunshandake, Horqin, and Songnen) and the NMTP (Fig. 3). The ϵNd of the peat samples
279 ranges between -0.5 and -9.8, while the $^{87}\text{Sr}/^{86}\text{Sr}$ varies from 0.704687 to 0.715998 (Fig. 3 and
280 Table S3).

281 The ϵNd of local sources (1.7 for rock and 1.1 for scoria; average of 1.5) is higher than the Chinese
282 drylands (average of -8.9 and -10.7 for NED and NMTP deserts respectively), while the $^{87}\text{Sr}/^{86}\text{Sr}$
283 is lower (0.704418 (rock) and 0.704555 (scoria) for an average of 0.704544 vs. 0.711065 (NED)
284 and 0.723295 (NMTP)) (Fig. 3, S2 and S3, Tables S2). The deserts of the Ordos Plateau as well
285 as the Badain Jaran and Tengger (isotopically part of the NMTP) have been invoked as a potential
286 source of dust in the region (Zaarur et al., 2020). While the Ordos Plateau cannot be completely
287 excluded as a minor source, the isotopic composition of the Hani samples is closer to the Badain
288 Jaran and Tengger, which are geographically near the Ordos Plateau. A number of samples in the
289 Hani record, mainly around 1.7, 10.7 and 13.0 cal ka BP, show a clear local signature (Fig. 2, 3,
290 5). Samples centered around 1.7 and 10.7 cal ka BP correspond in timing with volcanic eruptions
291 from the Jinlongdingzi volcano, located ~14km NW, and recorded in several records in the region
292 (Liu et al., 2009; Zhao et al., 2017). No eruptions have been reported around 13.0 cal ka BP, but
293 tephra layers dated around 11.4 and 14.0 cal ka BP and geochemically linked to the Longgang
294 volcanic field suggest there were some active volcanoes during that period (Liu et al., 2009).
295 Another potential explanation for the lower $^{87}\text{Sr}/^{86}\text{Sr}$ and higher Eu anomalies and grain size
296 around 13.0 cal ka BP, are flooding event or increased runoff from the surroundings of the peatland.
297 Hani peatland was not as developed at that time and the coring location was closer to the edge of
298 the peatland (Zhang et al., 2019), potentially resulting in a greater influx of local material at least
299 sporadically. While the presence of volcanic glasses in the corresponding layers could not be
300 confirmed given the limited amount of sample available, the clearly distinct signal in these layers
301 and correspondence with local volcanic sources suggest Nd and Sr isotopes can help pinpoint
302 volcanic eruptions (Le Roux et al., 2012) without having to find glass shards. Hence, they can be
303 used as complementary tools to classical tephrostratigraphy.

304 The NE drylands dominate as a source since the Late Pleistocene (Fig. 3 and 5). The contribution
305 of dust from the different sources was relatively stable except around 1.7 cal ka BP (local
306 sources: >58%) and between 1.8-4.0 cal ka BP (NMTP sources: 41%) (Fig. 3 and 5). This
307 dominance of dust from the NED is supported by modern dust observations. Modeling of dust
308 emission in northern China between 2001-2014 shows that Inner Mongolia is a significant source
309 (Du et al., 2018). Between 2000-2002, meteorological data shows that 8-30% of dust storm events
310 originated in eastern Inner Mongolia (Hunshandake, Horqin) (Zhang and Gao, 2007). Isotopic and
311 elemental geochemistry on Quaternary loess deposits in NE China (Xie et al., 2019; Zeng et al.,
312 2020) points to the Hunshandake and Horqin deserts (Fig. 1) as the main sources of the dust in the
313 region. While a large part of the samples displays a similar composition, some show slightly higher
314 $^{87}\text{Sr}/^{86}\text{Sr}$ than the loess. This can likely be explained by the Hani peatland location, i.e. at further
315 distances from the NED than the loess deposits and in a mountain range, the Changbai Mountains,
316 that likely partially intercept a portion of dust from those drylands. This difference in location
317 likely results in Hani peatland being more sensitive to contributions in dust from the NMTP.
318 Excluding the peak potentially related to volcanic eruptions, the proportion of dust from the NED
319 was greater prior to 10.0 cal ka BP.

320 Sr-Nd isotopes of the siliciclastic material from lake Sihailongwan (Zaarur et al., 2020), located to
321 the northeast of Hani peatland, display a slightly different composition with higher ϵNd and lower
322 $^{87}\text{Sr}/^{86}\text{Sr}$ (Fig. 3). Lake Sihailongwan is a maar lake developed in a volcanic crater, more likely to
323 receive more local material from the crater rims, which could explain the different Sr-Nd
324 composition between the two sites. This is supported by the higher Eu/Eu anomalies of the clastic
325 material of lake Sihailongwan ($\text{Eu}/\text{Eu}^*\text{PAAS} = 1.15$) in comparison to Hani ($\text{Eu}/\text{Eu}^*\text{PAAS} = 1.05$)
326 suggesting a greater proportion of volcanic material in the former. Such a difference in the
327 proportion of locally derived material would be enough to explain the difference in Sr-Nd isotope
328 composition between the two records. Other regional records, including lake Tuofengling, lake
329 Tianchi and Motianling peatland further north and northwest of Hani peatland (Fiałkiewicz-Kozieł
330 et al., 2022; Zhang et al., 2017; Zhou et al., 2023). Lake Tuofengling and Tianchi display
331 composition closer to the Mongolian Plateau, which Zhang et al. (2023) explains by the more
332 northern location of the two sites reducing the influence of the Westerlies on dust supply at those
333 sites. Motianling peatland Sr-Nd composition is also similar to that of the Mongolian Plateau and
334 the Hulun Buir sandy land which can be explained by its closer proximity to the two sources
335 (Fiałkiewicz-Kozieł et al., 2022). In summary, the Sr-Nd isotope and REE composition suggest
336 that the NE drylands of China, likely the Hunshandake and Horqin, are the main source of dust in
337 Hani peatland.

338

339 4.2 Influence of the East Asian monsoon on the dust inputs

340 Dust flux values in the Hani record are high during the Late Pleistocene and gradually decrease
341 starting at the early Holocene, a minimum is observed between 8.0-6.0 cal ka BP, followed by two
342 peaks at 5.8-3.8 and 1.7-0.3 cal ka BP (Fig. 6D and 7K). Change point analysis on the dust flux
343 from NED identified four changes (>99% confidence level) in the record at 1.8, 3.8, 5.7 and 11.9
344 cal ka BP. Some slight differences are present between the REE-based dust flux (Fig. D; white and

345 grey curve) and the NED dust flux (Fig. 6D; green curve). This is mainly attributable to the lower
346 sampling resolution of the Sr-Nd analyse and the fact that the REE-based dust flux represents the
347 total flux. For example, the peak found around 12.0 cal ka BP and 1.7 cal ka BP are not as
348 prominent in the NED flux record because the influence of local volcanic material was removed.
349 As demonstrated by the Sr-Nd isotopes analyses, the dust in Hani peatland is largely derived from
350 the NE drylands (the most likely sources being the Hunshandake and Horqin), so we focus on
351 climatic and environmental records from that region for comparisons. The good agreement
352 between the Hani dust record and the EASM dynamics has been highlighted in previous work
353 (Pratte et al., 2020). A potential influence of the EAWM and WJ on the Hani record was also
354 proposed, but the extent of that influence could not be properly assessed earlier without a more
355 detailed source tracing. Here, the Sr-Nd isotopes analyses allow for a more in depth understanding
356 of the factors influencing the Hani dust record.

357 The dominance of dust from the NE drylands is generally in accordance with the winter/spring
358 winds from the EAWM. Dust emission from the Gobi desert and the NE drylands is mainly
359 transported by near-surface northwesterly winds to proximal and intermediate regions (Sun et al.,
360 2001). The Hani dust record was compared to EAWM records from north China (Li and Morrill,
361 2015) and south China (Wang et al., 2012). These two records have good chronostratigraphic
362 constraints, cover most of the period of the Hani record and are strongly correlated to modern
363 EAWM index (Wang et al., 2012) or supported by transient simulations (Li and Morrill, 2015).
364 Peaks in dust deposition in Hani largely occur when EAWM intensity is lower in those records
365 (Fig. 7B and K), especially during the late- and mid-Holocene, suggesting that changes in the
366 deposition rate of dust in Hani are unlikely to be directly or solely related to EAWM intensity.
367 Furthermore, the particle grain size in the Hani record is quite stable, with several peaks coeval
368 with Sr-Nd signatures and Eu/Eu* anomalies (especially around 1.7, 10.7 and 13.0 cal ka BP; Fig.
369 5 and S1) closer to local volcanic sources. If changes in EAWM-related wind intensity were the
370 main driver of the Hani dust record, greater particle grain sizes would be observed during the late
371 Holocene and between 5.7-3.8 cal ka BP. Changes in the extent of the arid areas or frequency of
372 dust storms in the source region, also potentially related to the EAWM intensity and the Siberian
373 High (Roe, 2009), are more likely explanations for the dust deposition changes in the Hani record.
374 However, the long-term trend in EAWM intensity is opposite to the Hani dust flux, suggesting the
375 EAWM played a limited role at least over the last 10 cal ka BP, a relationship also evidenced in
376 other records (Chen et al., 2021b). There are discrepancies between EAWM records. Some display
377 different patterns with a gradual increase in EAWM strength from the Early to the Late Holocene
378 (Kang et al., 2020; Yang and Ding, 2008), while others display a strong EAWM in the Early and
379 Late Holocene and a weakening in the mid-Holocene (Liu et al., 2020; Yang and Ding, 2014, Xia
380 et al., 2014), a pattern more similar to the Hani dust flux. Discrepancies in reconstructions of
381 EAWM variations are mostly related to chronological uncertainties, proxy sensitivity and sediment
382 resolution. For example, several loess records present hiatus (Kang et al., 2020) or do not possess
383 direct chronologies (Yang and Ding, 2014), especially during the Holocene. Furthermore, loess
384 records on the Chinese Loess Plateau, are not only affected by EAWM changes but also EASM
385 changes (Yang and Ding, 2008), affecting source distance (advance/retreat of desert boundary)
386 (Ding et al., 2005) as well as sediment availability (Stevens et al., 2011), which also influence
387 loess grain size. Diatom-based (south China) and grain size-based (north China) EAWM records

388 (Li and Morrill, 2015; Wang et al., 2012) indicate a stronger EAWM in the Early Holocene (Fig.
389 7B), which could partially explain the higher dust flux and proportion from NED during that period.
390 The high dust deposition during the last 2.0 cal ka BP could also be partially explained by an
391 increase in EAWM as suggested by some records (An et al., 2011; Kang et al., 2020). Nevertheless,
392 while the EAWM likely plays a role in dust mobilization and transport, its relationship with the
393 Hani dust record is limited for most of the Holocene.

394 Changes in the Hani dust record, especially the gradual decrease in dust deposition from the Late
395 Pleistocene to a minimum between 8.0-6.0 cal ka BP (Fig. 6D), are consistent with EASM
396 variability, which controls precipitations (Fig. 6B). In contrast, precipitation records in NE China
397 (Jilin, Liaoning, and Heilongjiang provinces; Fig. 6A) display a distinct pattern than the EASM
398 margin and the Hani dust flux suggesting limited contribution from the region in terms of dust.
399 This contrast in the EASM precipitation between western (EASM margin) and NE China has
400 previously been observed (Zhang et al., 2018b; Zhou et al., 2016). Hence, for clarity we refer to
401 NE China as the region encompassing Liaoning, Jilin and Heilongjiang provinces and the NE
402 drylands (NED) as the drylands along the EASM margin. Moisture and precipitation level are
403 important factors controlling dust emission from drylands by affecting soil moisture and vegetation
404 cover in source regions (Tsoar and Pye, 1987). The evolution (stabilization/reactivation) of the
405 dune fields of the NED (Fig. 6C), located at the margin of the EASM (Fig. 1A), was driven by
406 monsoon precipitations since the Late Glacial (Xu et al., 2020). Dune activity was widespread in
407 the eastern drylands of China during the Late Pleistocene (Yang et al., 2019), the first evidence of
408 dune stabilization being recorded from ~11 cal ka BP. In three drylands of the region (Mu Us,
409 Hunshandake and Horqin; Fig. 1A), the proportion of stabilized dunes increased progressively to
410 reach a maximum around 6.0 cal ka BP (Fig. 6C), the dunes being largely vegetated at that time
411 (Lu et al., 2013). A migration of the monsoon rain belt, up to 400 km to the northwest (Chen et al.,
412 2021a; Goldsmith et al., 2017), along with a ~200 km NW retreat of deserts of northern China (Li
413 et al., 2014) culminating in the mid-Holocene has been proposed. A decrease in monsoonal
414 precipitations and vegetation cover along the EASM margin (Fig. 6B) and related increase dune
415 field activity (Fig. 6C) during the late Holocene are also reflected by an increase in dust deposition
416 in the Hani record (Fig. 6D). The Hani dust record shows an inverse relationship with the general
417 EASM trend along the EASM margin (Fig. 6B and S4), a relationship apparent elsewhere in
418 northern China where a negative correlation of dust with EASM precipitation and vegetation cover
419 was observed (Chen et al., 2021b). During periods of stronger EASM, such as between 6-8 cal ka
420 BP, more precipitation occurs over the NED resulting in a revegetation and stabilization of the
421 dune fields hence generating less dust. This would explain the lower dust deposition rates in Hani
422 peatland during the mid-Holocene. In contrast, the late Holocene drying and southward migration
423 of the EASM and boundary of drylands resulted in a reactivation of the dune fields and in an
424 increase in dust emission reflected by an increase of dust deposition in Hani peatland. This suggests
425 that EASM precipitation and vegetation cover are important control factors of the dust cycle in the
426 region.

427

428 4.3 Influence of the WJ on dust variability

429 The presence of a significant proportion of dust originating from the NMTP deserts (Fig. 3 and 4)
430 in Hani implies an influence of the WJ on dust supply and climate dynamics in the region. The
431 dust flux originating from the NMTP displays an increase after 6 cal ka BP, especially during the
432 late Holocene (Fig. 7K). Change-point analysis on the NMTP dust flux identified a change
433 significant at >99% at 5.8 cal ka BP. The increase in the NMTP dust flux since 6 cal ka BP also
434 supports a stronger WJ, in line with several WJ records in northern China (Fig. S6A-G). Changes
435 in dust flux have been linked to changes in the strength of the WJ and aridity in the source regions
436 (Ferrat et al., 2012; Lim and Matsumoto, 2008; Sun et al., 2004). Meteorological data have shown
437 that the WJ intensity tends to increase in years of greater dust storm frequency and intensity in
438 Central China (Zhong and Li, 2005). The position of the WJ can also exert an influence on dust
439 deposition in records. The WJ passing over dust source regions for a longer duration of time would
440 result in increased dust uplifting by the WJ, mobilizing more dust, and greater dust deposition
441 downwind (An et al., 2012; Lim and Matsumoto, 2008; Nagashima et al., 2007).

442 The WJ pathway migrates seasonally through East Asia, being south of the Himalaya (<30°N) in
443 winter and north of the Tibetan Plateau in summer (>42°N) (Schiemann et al., 2009). Recently,
444 evidence points to a control of the seasonal northward position and orientation of the WJ on the
445 EASM rainfall (Chiang et al., 2015; Herzschuh et al., 2019) and by extension on dust (Nagashima
446 et al., 2013). The strength and latitudinal position of the WJ has varied during the Holocene and
447 Late Pleistocene (Herzschuh et al., 2019; Nagashima et al., 2013). Variations in the WJ position
448 were previously reported (Nagashima et al., 2007; Nagashima et al., 2013) using electron spin
449 resonance (ESR) records from sediments from the Sea of Japan (Fig. 7I). Larger ESR values
450 indicate greater inputs from the Mongolian Gobi/NED, reflecting a southward position of the WJ.
451 The WJ was found to be located further south during the Late Pleistocene and between 5.5-3.5 and
452 1.5-0 cal ka BP affecting the northward extent of the EASM rainbelt (Nagashima et al., 2013).
453 This process could explain the more short-lived peaks in dust flux from NED in Hani, especially
454 between 5.7-3.8 and 1.8-0.3 cal ka BP (Fig. 7K). Several records in the region suggest that the WJ
455 was located further south approximately during the periods of high dust deposition in Hani
456 peatland (Fig. 7G-J). High dust flux periods (Fig. 7J) concurrent with changes in dust composition
457 were found to be related to a southward migration of the summer WJ and changes in land exposure
458 in NW Iran (Sharifi et al., 2015; 2018), while cooling of surface temperatures in the Yellow Sea
459 and mid-latitude Asia were explained a southward migration of the WJ during the same periods
460 (Bae et al., 2020). The relationship between the Hani dust record (Fig. 7K) and EASM rainfall
461 along the EASM margin (Fig. 7C-F) as well as the influence of the WJ, suggest that the Hani dust
462 flux was affected by both the WJ and EASM precipitations. A strengthening or intensification of
463 the WJ is often observed in concurrence with a southward/southeastward shift of its axis (An et
464 al., 2012; Herzschuh et al., 2019). This is confirmed by modelling experiments observing a
465 southward migration and intensification of the summer WJ over Central Asia from 6.5 cal ka BP
466 to the late Holocene with a brief return to a more northward position between 3-2 cal ka BP (Fig
467 7G; (Zhou et al., 2020). A more southward position of the WJ (Fig. 7G-I) would reduce rainfall at
468 the EASM margin (Fig. 7C-F), resulting in drier conditions in the main dust source region,
469 promoting dust emission from the NE drylands. Several EASM precipitation records near the NE
470 drylands (Fig. 7D-E) display drier conditions suggesting a southeastward retreat of the EASM (Fig.
471 7F; Wang et al., 2020) between 6.0-4.1 cal ka BP and 2.0-0 cal ka BP when the WJ is further south

472 and the NED dust deposition in Hani high (Fig. 7K) This interaction between the WJ and EASM
473 would explain the peak in dust observed at 5.8-3.8 and 1.6-0.3 cal ka BP in Hani. Furthermore,
474 with the WJ being further south, the influence of the EAWM is heightened (Nagashima et al.,
475 2007), without having to invoke an intensification, explaining the occurrence of high dust inputs
476 during periods of weaker EAWM. For the Early Holocene and Late Pleistocene, an intensified
477 EAWM (Fig. 7B) combined with a more southward WJ would also have increased the strength of
478 the NW winds resulting in more dust from the NED, but also in greater dust fluxes (Fig. 7K) along
479 with the relatively greater grain size prior to 10 cal ka BP.

480 The Sr-Nd isotopes record from Hani peatland (Fig. 3 and 5) displays less variability than the ESR
481 records from the Sea of Japan (Fig. 7I) and the isotopic composition of the dust in Neor peatland
482 in Iran (Sharifi et al., 2018). This is likely explainable by the more southerly location of the records
483 from the Sea of Japan (37°04'N) and Iran (37°57'N), making them more sensitive to WJ path
484 changes. Nevertheless, the dust flux record from Hani peatland show striking similarities with the
485 ESR records from the Sea of Japan and the dust flux from Neor peatland in Iran (Fig. 7J).
486 Nagashima et al. (2013) argue that changes in aeolian dust in the Sea of Japan reflect changes in
487 WJ path rather than changes in humidity over the Taklamakan and Mongolian Gobi during the
488 Holocene. While humidity over the Taklamakan and Mongolian Gobi might have not changed
489 significantly, conditions in the northeastern drylands of China, located along the EASM margin
490 and where a large fraction of the dust in Hani peatland is derived from, have changed with a similar
491 timing as the ESR and the Hani dust flux records (Fig. 6 and 7).

492 Although insolation, through the thermal gradient between high and low latitudes, is the dominant
493 factor explaining changes in the WJ and EASM (Marzin et al., 2013), the spatiotemporal
494 heterogeneity in the Holocene EASM rainfall pattern suggests other paleoclimatic factors also
495 have an effect (Chiang et al., 2015). The timing of the gradual diminution in the dust flux and
496 subsequent mid-Holocene minimum agrees with the overall decrease in ice volume over the early
497 Holocene, reaching a similar extent as today by 7 cal ka BP (Fig. 7A). A notable feature that can
498 be drawn from various paleorecords is that the maximum in EASM (mid-Holocene) in north-
499 central and NE China lags the early-Holocene maximum in insolation (An et al., 2000; Chen et al.,
500 2015). The presence of remnant ice sheets in the Northern Hemisphere (Fig. 7A) is a potential
501 factor for this lag (Marzin et al., 2013) by obstructing the northward migration and deviating the
502 path of the WJ and by extension the EASM front in northern China. Furthermore, the presence of
503 the ice sheet, resulting in lower temperatures in Siberia (Bush, 2005), would have strengthened the
504 Siberian High, possibly contributing to the weakening of the EASM and strengthening of the
505 EAWM during the early Holocene. Other proposed mechanisms include freshwater inputs in the
506 North Atlantic causing a weakening of the AMOC or more frequent El Niño events (especially for
507 the late Holocene), both strengthening the WJ, thereby weakening the EASM (Chen et al., 2015).

508 Dust is controlled by several factors and its variability is unlikely to be solely attributed to the
509 changes in EASM intensity and the WJ. Some discrepancies between records can be explained by
510 the type of proxy as well as the nature of the records used which each encompass the climatic and
511 dust signal differently. Furthermore, aeolian dust deposition is spatially heterogenous in nature
512 and different factors such as vegetation at the source and deposition site, precipitation amounts at

513 the study sites, or sedimentation process in the case of lacustrine and marine records will affect
514 the final proxy records and result in potential discrepancies.

515 In addition to these controlling climatic factors, human activities have increasingly been
516 recognized as a potential contributing factor on the dust cycle in northern China, especially over
517 the last 2 cal ka BP. A dust storm record from lake Gonghai, on the Chinese Loess Plateau, suggests
518 peaks in dust activity occurred during periods of higher monsoonal precipitation and human
519 population, leading the authors to argue for a change from a natural to an anthropogenic forcing
520 on dust over the last 2 cal ka BP in Asia (Chen et al., 2020; Chen et al., 2021b). Lake Gonghai is
521 located in the core area of ancient China with a long history of human occupation, which probably
522 explains the strong influence of human activities on the regional dust cycle. In contrast, human
523 occupation in the region surrounding the main dust source of our study was less prominent and
524 more variable (Guo et al., 2018). Population in Inner Mongolia and Jilin provinces remained near
525 or below 2 million peoples for most of the late Holocene (Fig. 8B). Prior to 0.75 cal ka BP, peak
526 in dust in Hani generally occurred during periods of lower population. Furthermore, for most of
527 the Holocene, period of greater density of archeological sites in NE China (Fig. 8), including the
528 near the drylands, often occur during periods of lower dust deposition in Hani. While a general
529 increasing trend in dust levels over the last 2 cal ka BP is a common feature of several records (He
530 et al., 2015; Wang et al., 2014; Xu et al., 2018), the centennial and decadal variations often display
531 different timing. Discrepancies with several other dust records suggest that the impact of human
532 activities on dust was still very regional in nature. Human activities, mainly millet agriculture,
533 were found to have affected dune dynamics in the Mu Us and Hobq deserts region starting around
534 2.5 cal ka BP, while the region around the Hunshandake, Horqin and Hulun Buir saw a later
535 development around 1.5 cal ka BP with more intensive activities after 1.0 cal ka BP (Guo et al.,
536 2019; Makohonienko et al., 2004). For example, He et al. (2015) suggest that human impacts on
537 vegetation coverage and dust would have remained secondary to climate factors prior to 250 a cal
538 BP on the NE Tibetan Plateau, as population size and agricultural activities would have been too
539 low in the region. Furthermore, satellite-based measurements of dust optical depth (MODIS) show
540 that 25% of modern global dust emission is of anthropogenic origin (Ginoux et al., 2012). It is
541 expected that late Holocene dust emissions from human activities were lower than modern
542 emissions. While human activities are likely to have increasingly contributed to the dust signal
543 over the late Holocene, especially over the last 1000 years, it is difficult to directly quantify their
544 influence on dust levels and it is premature to ascribe most of dust emissions in the region to human
545 impacts.

546

547 **4 Conclusions**

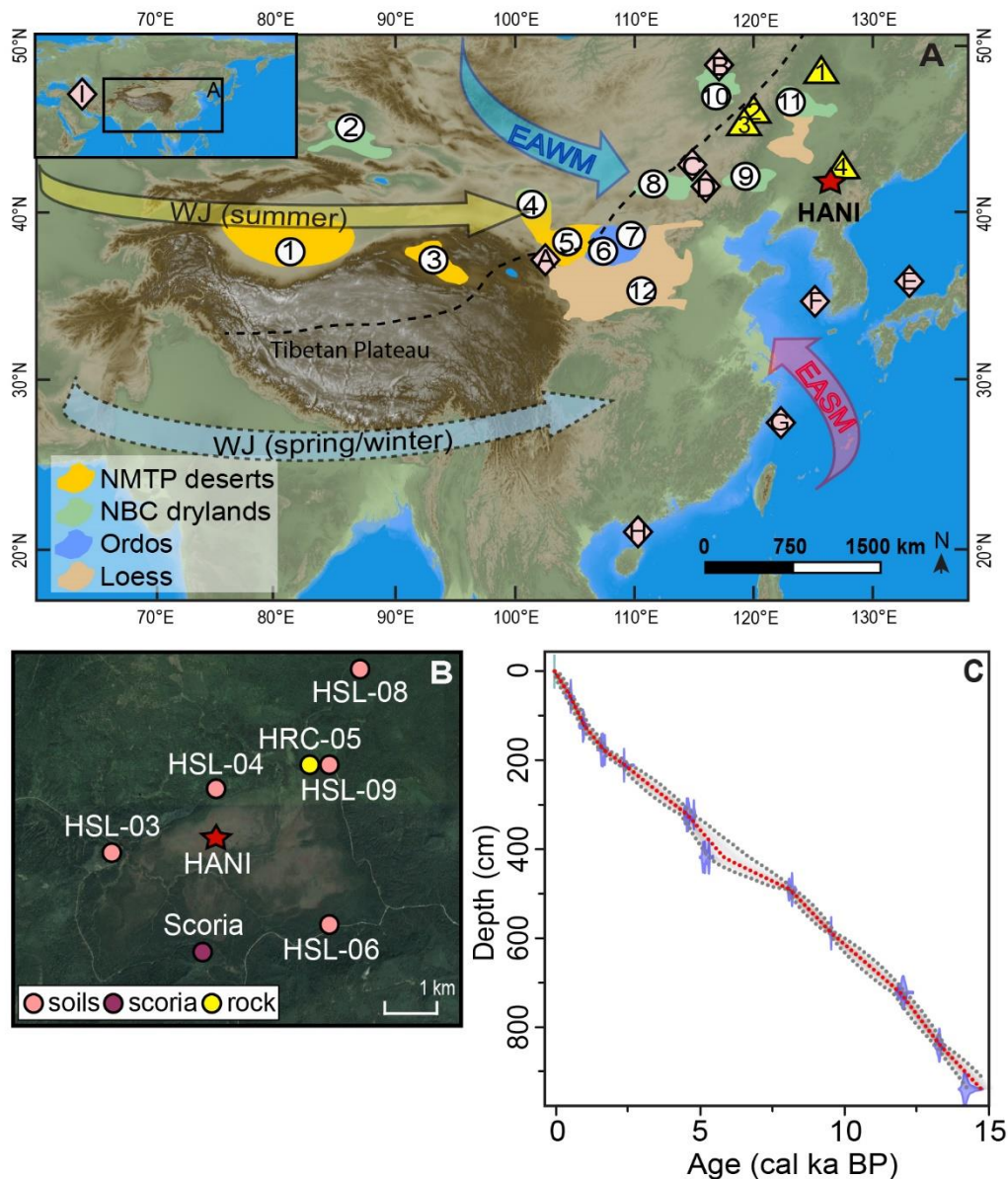
548 In this study, we presented a record of the Sr-Nd isotope composition of mineral dust covering the
549 last 14 cal ka BP in a peat sequence from the Changbai Mountains in NE China. The NE drylands
550 (Hunshandake, Horqin) were identified as the main source of the aeolian dust deposited in the
551 record, along with a contribution of the deserts along the northern margin of the Tibetan Plateau
552 (NMTP). The timing of the changes in dust deposition from NED follows the general pattern of
553 EASM precipitations along the EASM margin during the Holocene. The contribution of dust from

554 the NMTP also suggests an influence of the Westerly Jet on dust and climate dynamics in the
555 region. In summary, we argue that the dust in the Hani peatland likely reflects changes in the
556 surface conditions of the NE drylands (mainly Hunshandake and Horqin) related to variations in
557 EASM rainfall with an influence of the position of the WJ. A stronger and more southerly WJ
558 results in lower monsoonal rainfall over the NE drylands, which in turn increases dust loadings in
559 the region. In the context of the current global warming, changes in the thermal gradient between
560 high and low latitudes would affect the WJ position and strength not only modifying EASM
561 rainfall patterns, but also the dust cycle in the region.

562

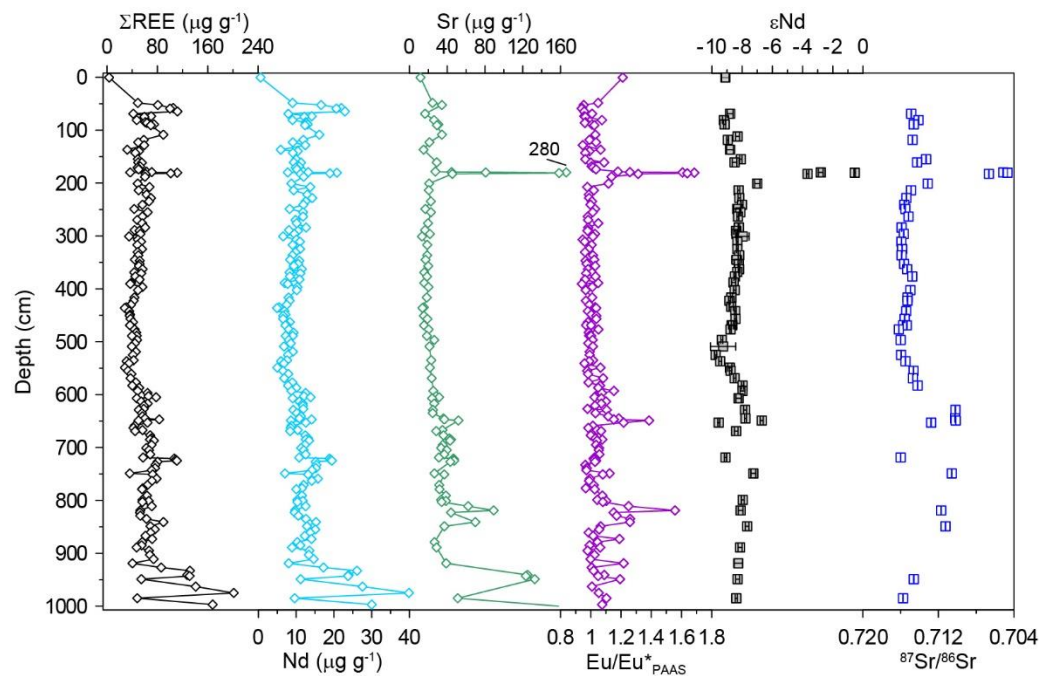
563 **Acknowledgments**

564 The ICP-MS & TIMS services of OMP (A. Lanzanova, C. Duquenoy, S. Mounic) as well as M.-
565 J. Tavella (LEFE) are acknowledged for help with sample preparation and ICP-MS measurements.
566 This research was supported by the Chinese Academy of Sciences President's International
567 Fellowship Initiative (#2017PC0078) to SP, the National Nature Science Foundation of China
568 (NSFC; #41971113) to KB and the NSFC-CNRS Joint Research Project (#41611130163) to KB
569 and FDV. C.L acknowledges financial support from the Swiss National Science Foundation SPF
570 grant TMPFP2_210183.



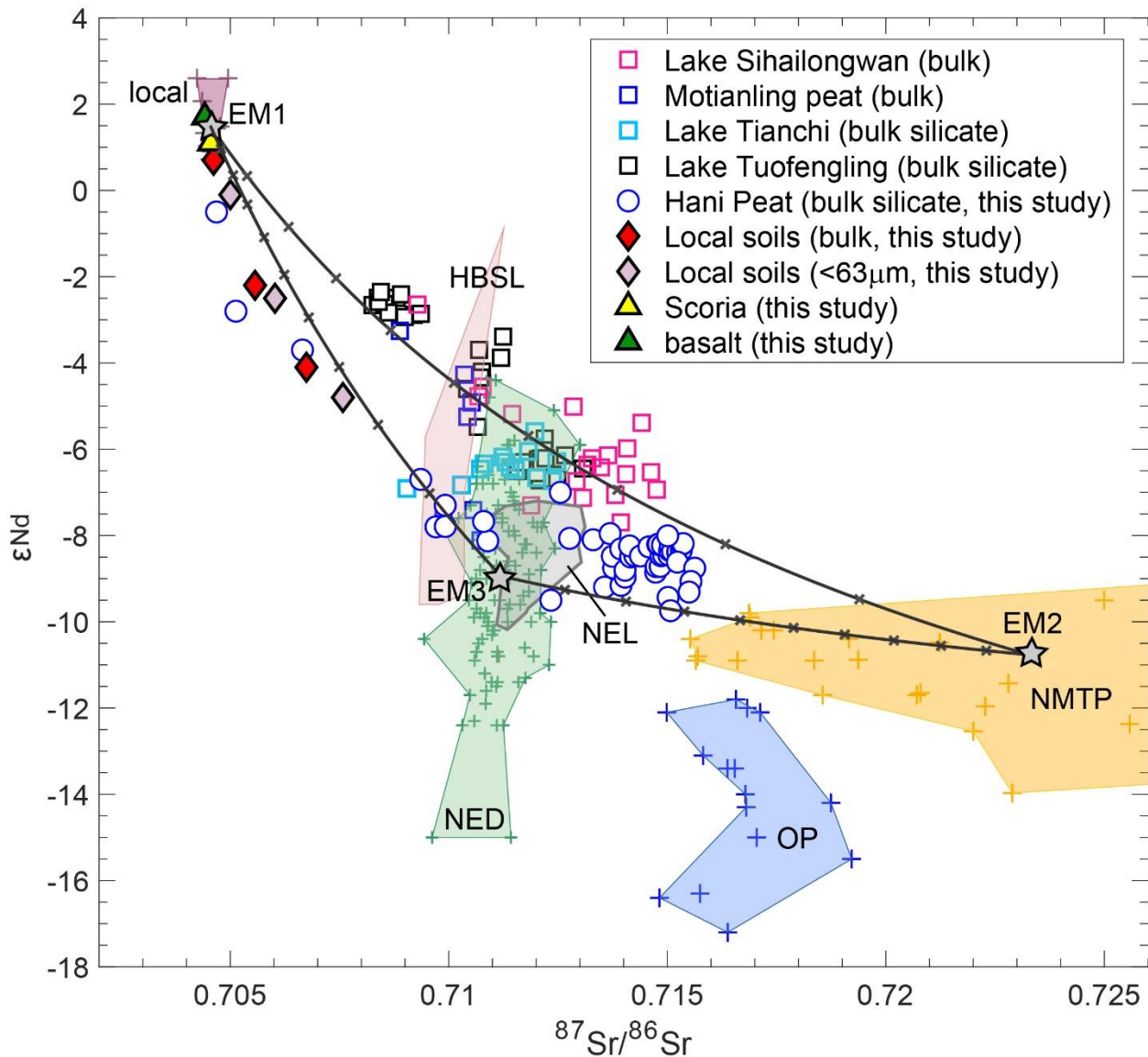
571

572 **Figure 1.** Location of the study region and study site. A) Chinese deserts and drylands (circles). 1.
 573 Taklamakan; 2. Gurbantunggut, 3. Qaidam; 4. Badain Jaran; 5. Tengger; 6. Mu Us; 7. Hobq; 8.
 574 Hunshandake; 9. Horqin; 10. Hulun Buir; 11. Songnen; 12. Chinese Loess Plateau. Diamonds:
 575 relative location of the records discussed in the text: A. Huangyang lake; B. Lake Hulun; C. Lake
 576 Bayanchagan; D. Chifeng Loess section, NE China; E. sediment cores D-GC-6 and MD01-2407,
 577 Sea of Japan; F. cores HMB-102/HMB-103, SE Yellow Sea; G. core MD06-3040, East China Sea;
 578 H. Huguang Maar lake; I. Neor peatland, Iran. Triangles: regional Sr-Nd isotopes records: 1. Lake
 579 Tianchi; Lake Tuofengling; 3. Motianling peatland; 4. Lake Sihailongwan. Black dashed line:
 580 relative modern limit of the EASM, Chen et al. 2008). NMTP: northern margin of the Tibetan
 581 Plateau, NBC: northern boundary of China. Arrows: General trajectories of the main wind systems.
 582 B) Location of the Hani-3 core and local sources. C) Age-depth model of the Hani-3 core (details
 583 in Pratte et al. (2020)).



584

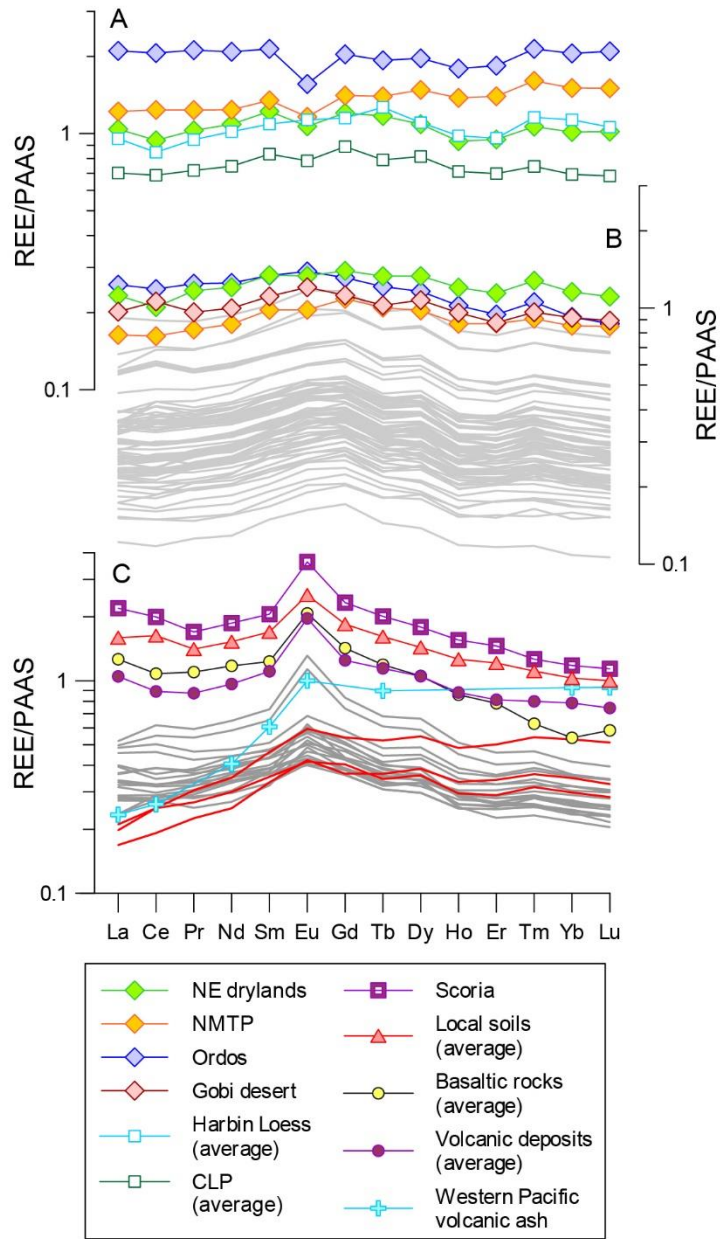
585 **Figure 2.** Summary of key data from Hani-3 peat core. Total REE (ΣREE), Nd and Sr
 586 concentrations ($\mu\text{g g}^{-1}$), $\text{Eu}/\text{Eu}^*_{\text{PAAS}}$ (normalized to Post-Archean Australian shale) (Pratte et al.,
 587 2020), ϵNd (this study) and $^{87}\text{Sr}/^{86}\text{Sr}$ (this study).



588

589 **Figure 3.** Comparison of ϵNd vs. $^{87}\text{Sr}/^{86}\text{Sr}$ of the dust in Hani samples with potential sources.
 590 Potential sources of Asian dust: Local (bulk basalts and scoria; Basu et al., 1991; Peng et al., 1986;
 591 Yan et al., 2007; Zaarur et al., 2020), NMTP (<75 μm ; Taklamakan, Qaidam, Tengger; Badain
 592 Jaran; (Chen et al., 2007a; Li et al., 2009), Ordos Plateau (OP: <75 μm Hobq, Mu Us; Chen et al.,
 593 2007a), and NE drylands (NED; Chen et al., 2007a; Xie et al., 2020), Hulun Buir sandy land
 594 (HBSL <10 μm , <30 μm and <63 μm ; Xie et al., 2017), Gobi (Yang et al., 2009)), NE loess (NEL;
 595 <10 μm , <30 μm and <63 μm ; Xie et al., 2019; Zeng et al., 2020). Regional records include lake
 596 Sihailongwan (Zaarur et al., 2020), lake Tianchi (Zhou et al., 2023), lake Tuofengling (Zhang et
 597 al., 2023) and Motianling peatland (Fiałkiewicz-Kozieł et al., 2022). Black lines: end member
 598 (stars) mixing lines between local sources (EM1), NMTP (EM2), and NED (EM3), with 10%
 599 increments denoted.

600

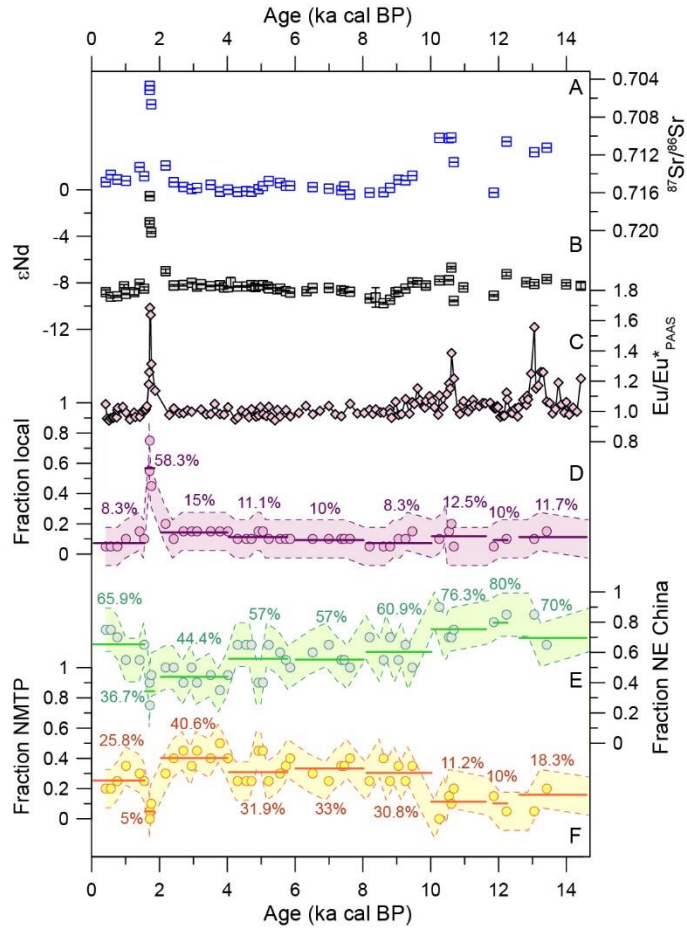


601

602 **Figure 4.** Rare earth element (REE) patterns of Hani peat samples (grey and red curves)
 603 normalized to the Post-Archean Australian shales (PAAS; Taylor and McLennan, 1985).
 604 Comparison with average composition of <75 μm (A) and fine <5 μm (B) fractions of deserts/dune
 605 fields (diamonds: Ferrat et al., 2011; Hu and Yang, 2016; Jiang and Yang, 2019; Rao et al., 2011;
 606 Xie et al., 2019; Xie et al., 2017; Zhang et al., 2018a) and loess (squares: Ferrat et al., 2011; Xie
 607 et al., 2017); (C) average composition of local sources: soils, volcanic rocks and volcanic deposits
 608 (triangles and dots: this study; Chen et al., 2007b; Liu et al., 2009; Schettler et al., 2006b) and
 609 volcanic ash (cross: Bailey, 1993).

610

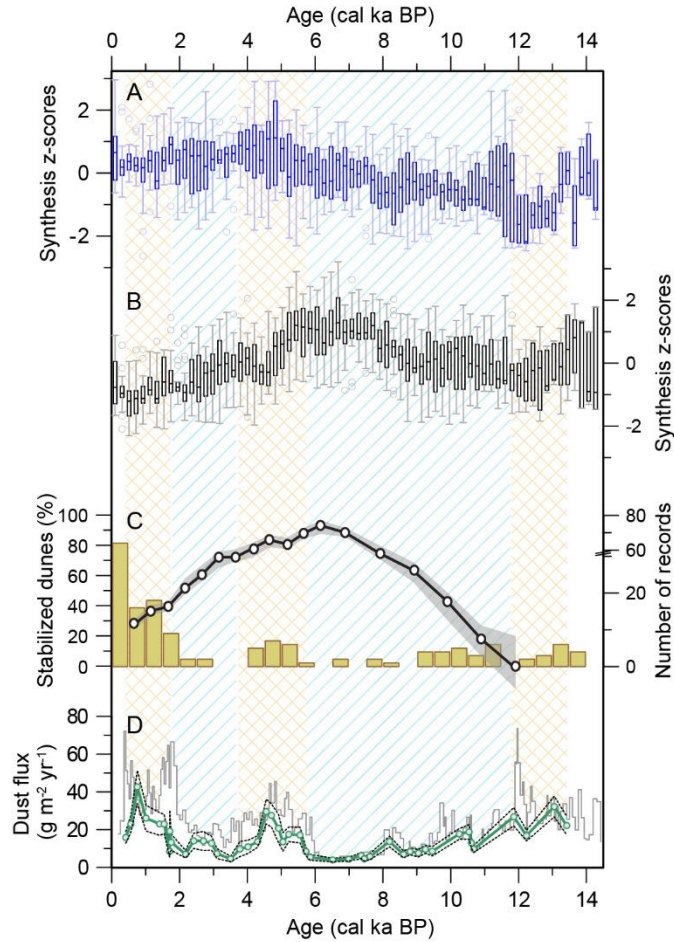
611



612

613 **Figure 5.** (A) $^{87}\text{Sr}/^{86}\text{Sr}$, (B) ϵNd , (C) Eu/Eu^* normalized to PAAS (Pratte et al., 2020), and the
 614 fraction of dust from end-members EM1 (D), EM2 (E) and EM3 (F). Dashed lines and colored
 615 area (D, E, F) represent 1σ uncertainty. Lines in D, E, and F represent average values for each
 616 period (1-9) identified in Fig. S1.

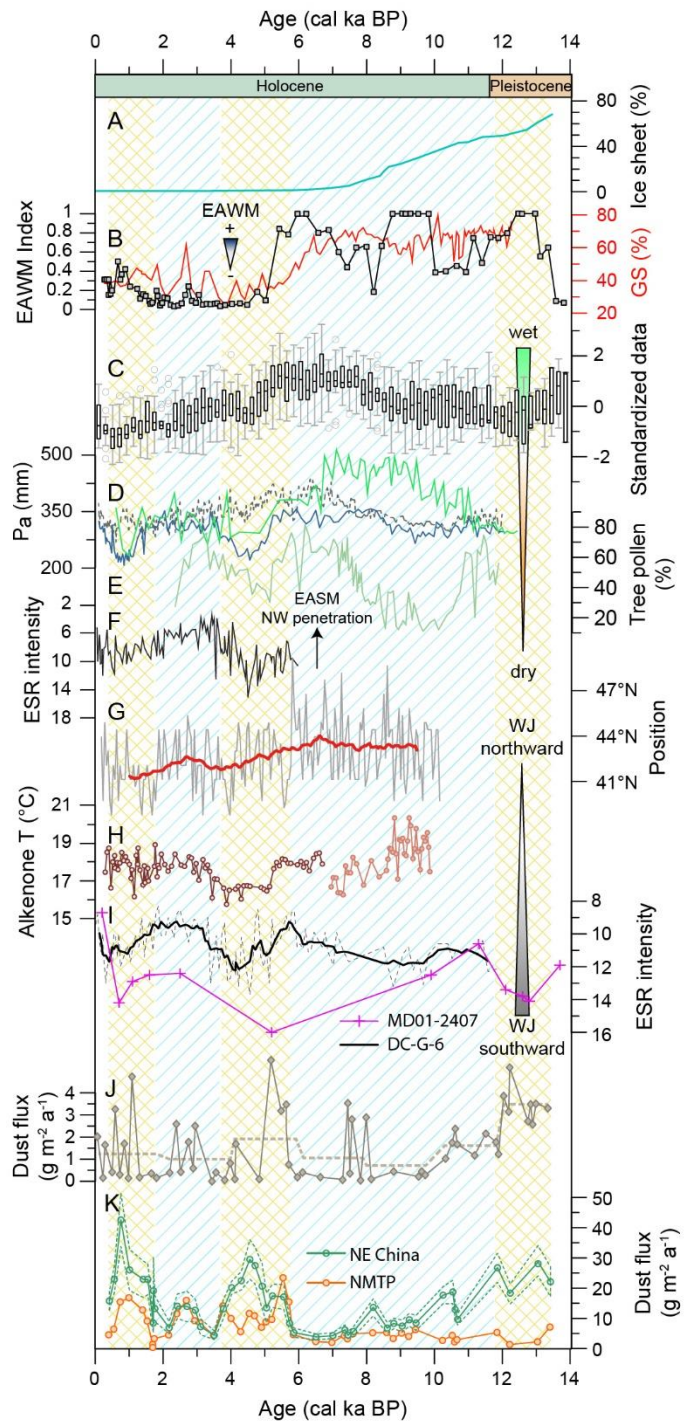
617



618

619 **Figure 6.** Comparison of the Hani record with records of surface conditions. A) Synthesized
 620 humidity/precipitation records for the eastern part of NE China (n=6; from Fig. S5) and B) the
 621 EASM margin (n=8; from Fig. S4); C) % of stabilized dunes relative to total in the drylands of
 622 northern China (Hunshandake, Horqin, Mu Us; black curve) (Xu et al., 2020) and number of
 623 records with mobile dune dates in NE drylands (Hunshandake, Horqin and Hulun Buir; histograms
 624 (Guo et al., 2019; Xu et al., 2020); D) REE-based total dust flux (grey step line) and dust flux from
 625 NE drylands (green) in Hani-3 core, dashed lines: uncertainties to 1σ . Yellow (higher dust
 626 deposition) and blue (lower dust) zones were identified based on change-point analysis.

627



628

629 **Figure 7.** Comparison of the Hani dust record with climatic records. A) % remnant ice sheet in
 630 the Northern Hemisphere (Dyke, 2004). B) EAWM intensity indexes: diatom-based index of
 631 EAWM intensity from Huguang maar lake (Wang et al., 2012) and grain size-based (GS) index
 632 from Huangyang profile (red curve, Li and Morrill, 2015). EASM records: C) Synthesized
 633 precipitation record (n=8) from the EASM margin region (from Fig. S4); D) Pollen-based annual
 634 precipitation (P_a) reconstruction from Bayanchagan (green), Hulun lake (blue) (Wen et al., 2010)

635 and Dali lake (dashed line) (Wen et al., 2017); E) Tree pollen % from Diaojiao lake (Shi and Song,
636 2003); F) Electron spin resonance (ESR) record from core MD06-3040 from the East China Sea
637 (Wang et al., 2020). Indexes of Westerly latitudinal position (selected from Fig. S6): G) simulated
638 latitudinal position of the summer WJ in Central Asia (Zhou et al., 2020); H) Alkenone-based T
639 ($^{\circ}\text{C}$) record from the Yellow Sea (Bae et al., 2020). I) Electron spin resonance (ESR) intensity in
640 sediment cores from the Japan Sea (Nagashima et al., 2007; Nagashima et al., 2013). J) Ti
641 concentration-based dust flux (solid line) and 2000 years-averaged flux (dashed line) from Neor
642 peatland, Iran (Sharifi et al., 2015); K) Dust flux from NED (green) and NMTP (orange) in Hani-
643 3 core, dashed lines: uncertainties to 1σ . Yellow (higher dust deposition) and blue (lower dust)
644 patterns are the zones determined by change-point analysis on the Hani dust flux.

645

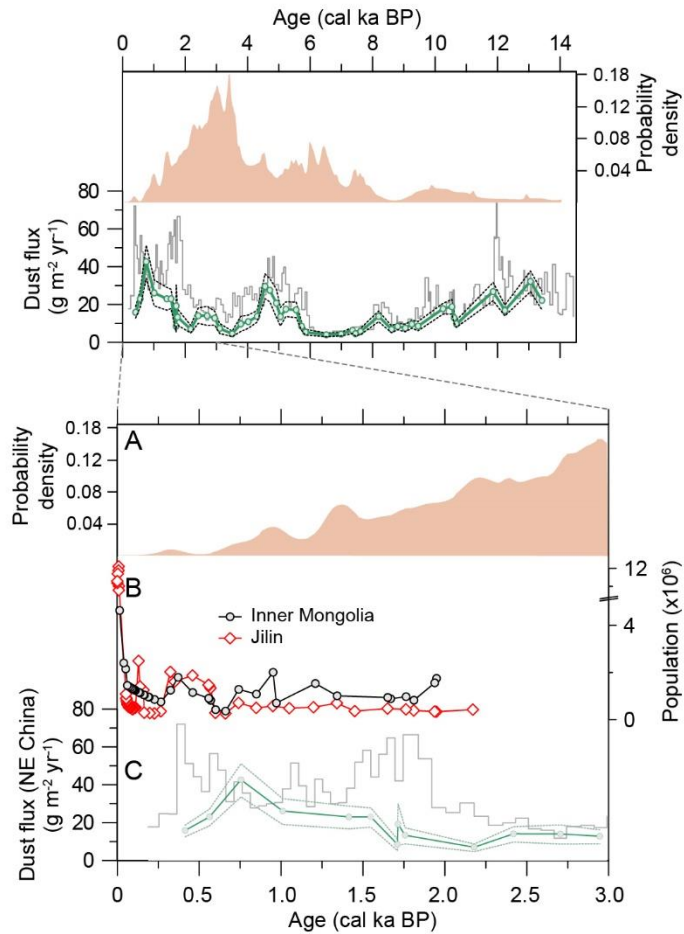
646

647

648

649

650



651

652 **Figure 8.** Bottom: Comparison of the Hani dust record with indicators of human activity in the
 653 dust source region and NE China. Top: probability density of archeological dates in NE China
 654 (including Hunshandake, Horqin) since 14 ka (Wang et al., 2021); Hani REE-based dust flux
 655 record. Bottom: A) Probability density of archeological dates in NE China (Wang et al., 2021); B)
 656 Historical records of population of the dust source region (Inner Mongolia) and the location of
 657 Hani peatland (Jilin) (Zhao and Xie, 1988; Song, 1987a, 1987b); C) Hani REE-based dust flux
 658 record.

659

660

661 **References**

- 662 Albarède, F., 1995. Introduction to geochemical modelling. Cambridge University Press, Cambridge.
 663 An, Z., 2000. The history and variability of the East Asian paleomonsoon climate. Quaternary Science
 664 Reviews 19, 171-187.
 665 An, Z., Colman, S.M., Zhou, W., Li, X., Brown, E.T., Jull, A.J.T., Cai, Y., Huang, Y., Lu, X., Chang, H., Song, Y.,
 666 Sun, Y., Xu, H., Liu, W., Jin, Z., Liu, X., Cheng, P., Liu, Y., Ai, L., Li, X., Liu, X., Yan, L., Shi, Z., Wang, X., Wu, F.,

667 Qiang, X., Dong, J., Lu, F., Xu, X., 2012. Interplay between the Westerlies and Asian monsoon recorded in
668 Lake Qinghai sediments since 32 ka. *Scientific Reports* 2, 619.

669 An, Z., Porter, S.C., Kutzbach, J.E., Xihao, W., Suming, W., Xiaodong, L., Xiaoqiang, L., Weijian, Z., 2000.
670 Asynchronous Holocene optimum of the East Asian monsoon. *Quaternary Science Reviews* 19, 743-762.

671 Bae, S.W., Lee, K.E., Chang, T.S., 2020. Two long and pronounced cold periods 3,000–5,000 and 6,600–
672 8,400 years B.P. in East Asia and the southward migration of the westerly jet. *Palaeogeography,*
673 *Palaeoclimatology, Palaeoecology* 537, 109402.

674 Bailey, J.C., 1993. Geochemical history of sediments in the northwestern Pacific Ocean. *Geochemical*
675 *Journal* 27, 71-90.

676 Basu, A.R., Wang, J., Huang, W., Xie, G., Tatsumoto, M., 1991. Major element, REE, and Pb, Nd and Sr
677 isotopic geochemistry of Cenozoic volcanic rocks of eastern China: implications for their origin from
678 suboceanic-type mantle reservoirs. *Earth Planet Sc Lett* 105, 149-169.

679 Beaudon, E., Sheets, J.M., Martin, E., Sierra-Hernández, M.R., Mosley-Thompson, E., Thompson, L.G., 2022.
680 Aeolian dust preserved in the Guliya ice cap (Northwestern Tibet): a promising paleo-environmental
681 messenger. *Geosciences* 12, 366.

682 Biscaye, P.E., Grousset, F.E., Revel, M., Van der Gaast, S., Zielinski, G.A., Vaars, A., Kukla, G., 1997. Asian
683 provenance of glacial dust (stage 2) in the Greenland Ice Sheet Project 2 Ice Core, Summit, Greenland.
684 *Journal of Geophysical Research: Oceans* 102, 26765-26781.

685 Bureau of Geology and Mineral Resource of Jilin Province (1988) *Regional Geology of Jilin Province*. Beijing:
686 Geological Press, pp. 698. (in Chinese).

687 Bush, A.B.G., 2005. CO₂/H₂O and orbitally driven climate variability over central Asia through the
688 Holocene. *Quaternary International* 136, 15-23.

689 Chen, F., Yu, Z., Yang, M., Ito, E., Wang, S., Madsen, D.B., Huang, X., Zhao, Y., Sato, T., John B. Birks, H.,
690 Boomer, I., Chen, J., An, C. and Wünnemann, B. (2008) Holocene moisture evolution in arid central Asia
691 and its out-of-phase relationship with Asian monsoon history. *Quaternary Science Reviews* 27, 351-364.

692 Chen, F., Chen, S., Zhang, X., Chen, J., Wang, X., Gowan, E.J., Qiang, M., Dong, G., Wang, Z., Li, Y., Xu, Q.,
693 Xu, Y., Smol, J.P., Liu, J., 2020. Asian dust-storm activity dominated by Chinese dynasty changes since 2000
694 BP. *Nature Communications* 11, 992.

695 Chen, F., Xu, Q., Chen, J., Birks, H.J.B., Liu, J., Zhang, S., Jin, L., An, C., Telford, R.J., Cao, X., Wang, Z., Zhang,
696 X., Selvaraj, K., Lu, H., Li, Y., Zheng, Z., Wang, H., Zhou, A., Dong, G., Zhang, J., Huang, X., Bloemendal, J.,
697 Rao, Z., 2015. East Asian summer monsoon precipitation variability since the last deglaciation. *Scientific*
698 *Reports* 5, 11186.

699 Chen, J., Li, G., Yang, J., Rao, W., Lu, H., Balsam, W., Sun, Y., Ji, J., 2007a. Nd and Sr isotopic characteristics
700 of Chinese deserts: Implications for the provenances of Asian dust. *Geochimica et Cosmochimica Acta* 71,
701 3904-3914.

702 Chen, J., Zhang, Q., Huang, W., Lu, Z., Zhang, Z., Chen, F., 2021a. Northwestward shift of the northern
703 boundary of the East Asian summer monsoon during the mid-Holocene caused by orbital forcing and
704 vegetation feedbacks. *Quaternary Science Reviews* 268, 107136.

705 Chen, S., Liu, J., Wang, X., Zhao, S., Chen, J., Qiang, M., Liu, B., Xu, Q., Xia, D., Chen, F., 2021b. Holocene
706 dust storm variations over northern China: transition from a natural forcing to an anthropogenic forcing.
707 *Science Bulletin* 66, 2516-2527.

708 Chen, Y., Zhang, Y., Graham, D., Su, S., Deng, J., 2007b. Geochemistry of Cenozoic basalts and mantle
709 xenoliths in Northeast China. *Lithos* 96, 108-126.

710 Chen, Z., Li, G., 2013. Evolving sources of eolian detritus on the Chinese Loess Plateau since early Miocene:
711 Tectonic and climatic controls. *Earth Planet Sc Lett* 371-372, 220-225.

712 Chiang, J.C.H., Fung, I.Y., Wu, C.-H., Cai, Y., Edman, J.P., Liu, Y., Day, J.A., Bhattacharya, T., Mondal, Y.,
713 Labrousse, C.A., 2015. Role of seasonal transitions and westerly jets in East Asian paleoclimate.
714 *Quaternary Science Reviews* 108, 111-129.

715 Chu, G., Sun, Q., Zhaoyan, G., Rioual, P., Qiang, L., Kaijun, W., Han, J., Liu, J., 2009. Dust records from
716 varved lacustrine sediments of two neighboring lakes in northeastern China over the last 1400 years.
717 *Quaternary International* 194, 108-118.

718 DePaolo, D.J., Wasserburg, G.J., 1976. Nd isotopic variations and petrogenetic models. *Geophysical*
719 *Research Letters* 3, 249-252.

720 Ding, Z.L., Derbyshire, E., Yang, S.L., Sun, J.M. and Liu, T.S. (2005) Stepwise expansion of desert
721 environment across northern China in the past 3.5 Ma and implications for monsoon evolution. *Earth*
722 *Planet Sc Lett* 237, 45-55.

723 Du, H., Wang, T., Xue, X., Li, S., 2018. Modelling of sand/dust emission in Northern China from 2001 to
724 2014. *Geoderma* 330, 162-176.

725 Dyke, A.S., 2004. An outline of North American deglaciation with emphasis on central and northern
726 Canada, in: Ehlers, J., Gibbard, P.L. (Eds.), *Developments in Quaternary Sciences*. Elsevier, pp. 373-424.

727 Feng, J.-L., Zhu, L.-P., Zhen, X.-L., Hu, Z.-G., 2009. Grain size effect on Sr and Nd isotopic compositions in
728 eolian dust: Implications for tracing dust provenance and Nd model age. *Geochemical Journal* 43, 123-
729 131.

730 Ferrat, M., Weiss, D.J., Spiro, B., Large, D., 2012. The inorganic geochemistry of a peat deposit on the
731 eastern Qinghai-Tibetan Plateau and insights into changing atmospheric circulation in central Asia during
732 the Holocene. *Geochimica et Cosmochimica Acta* 91, 7-31.

733 Ferrat, M., Weiss, D.J., Strekopytov, S., Dong, S., Chen, H., Najorka, J., Sun, Y., Gupta, S., Tada, R., Sinha,
734 R., 2011. Improved provenance tracing of Asian dust sources using rare earth elements and selected trace
735 elements for palaeomonsoon studies on the eastern Tibetan Plateau. *Geochimica et Cosmochimica Acta*
736 75, 6374-6399.

737 Fiałkiewicz-Kozieł, B., Bao, K., Smieja-Król, B., 2022. Geographical drivers of geochemical and mineralogical
738 evolution of Motianling peatland (Northeast China) exposed to different sources of rare earth elements
739 and Pb, Nd, and Sr isotopes. *Science of The Total Environment* 807, 150481.

740 Gaiero, D.M., Depetris, P.J., Probst, J.-L., Bidart, S.M., Leleyter, L., 2004. The signature of river- and wind-
741 borne materials exported from Patagonia to the southern latitudes: a view from REEs and implications for
742 paleoclimatic interpretations. *Earth Planet Sc Lett* 219, 357-376.

743 Gallet, S., Jahn, B.-m., Van Vliet Lanoë, B., Dia, A., Rossello, E., 1998. Loess geochemistry and its
744 implications for particle origin and composition of the upper continental crust. *Earth Planet Sc Lett* 156,
745 157-172.

746 Ginoux, P., Prospero, J.M., Gill, T.E., Hsu, N.C., Zhao, M., 2012. Global-scale attribution of anthropogenic
747 and natural dust sources and their emission rates based on MODIS Deep Blue aerosol products. *Reviews*
748 *of Geophysics* 50.

749 Ginoux, P., Prospero, J.M., Torres, O., Chin, M., 2004. Long-term simulation of global dust distribution with
750 the GOCART model: correlation with North Atlantic Oscillation. *Environmental Modelling & Software* 19,
751 113-128.

752 Goldsmith, Y., Broecker, W.S., Xu, H., Polissar, P.J., deMenocal, P.B., Porat, N., Lan, J., Cheng, P., Zhou, W.,
753 An, Z., 2017. Northward extent of East Asian monsoon covaries with intensity on orbital and millennial
754 timescales. *Proceedings of the National Academy of Sciences* 114, 1817-1821.

755 Goudie, A.S., 2009. Dust storms: Recent developments. *Journal of Environmental Management* 90, 89-94.

756 Grousset, F.E., Biscaye, P.E., Revel, M., Petit, J.-R., Pye, K., Joussaume, S., Jouzel, J., 1992. Antarctic (Dome
757 C) ice-core dust at 18 k.y. B.P.: Isotopic constraints on origins. *Earth Planet Sc Lett* 111, 175-182.

758 Guo, L., Xiong, S., Dong, X., Ding, Z., Yang, P., Zhao, H., Wu, J., Ye, W., Jin, G., Wu, W., Zheng, L., 2019.
759 Linkage between C4 vegetation expansion and dune stabilization in the deserts of NE China during the
760 late Quaternary. *Quaternary International* 503, 10-23.

761 He, Y., Zhao, C., Song, M., Liu, W., Chen, F., Zhang, D., Liu, Z., 2015. Onset of frequent dust storms in
762 northern China at ~AD 1100. *Scientific Reports* 5, 17111.

763 Herzsuh, U., Cao, X., Laepple, T., Dallmeyer, A., Telford, R.J., Ni, J., Chen, F., Kong, Z., Liu, G., Liu, K.-B.,
764 Liu, X., Stebich, M., Tang, L., Tian, F., Wang, Y., Wischnowski, J., Xu, Q., Yan, S., Yang, Z., Yu, G., Zhang, Y.,
765 Zhao, Y., Zheng, Z., 2019. Position and orientation of the westerly jet determined Holocene rainfall
766 patterns in China. *Nature Communications* 10, 2376.

767 Hu, F., Yang, X., 2016. Geochemical and geomorphological evidence for the provenance of aeolian
768 deposits in the Badain Jaran Desert, northwestern China. *Quaternary Science Reviews* 131, 179-192.

769 Jacobsen, S.B., Wasserburg, G.J., 1980. Sm-Nd isotopic evolution of chondrites. *Earth Planet Sc Lett* 50,
770 139-155.

771 Jiang, Q., Yang, X., 2019. Sedimentological and Geochemical Composition of Aeolian Sediments in the
772 Taklamakan Desert: Implications for Provenance and Sediment Supply Mechanisms. *Journal of*
773 *Geophysical Research: Earth Surface* 124, 1217-1237.

774 Kohfeld, K.E., Harrison, S.P., 2001. DIRTMAP: the geological record of dust. *Earth-Science Reviews* 54, 81-
775 114.

776 Kang, S., Du, J., Wang, N., Dong, J., Wang, D., Wang, X., Qiang, X. and Song, Y. (2020) Early Holocene
777 weakening and mid- to late Holocene strengthening of the East Asian winter monsoon. *Geology* 48, 1043-
778 1047.

779 Le Roux, G., Fagel, N., De Vleeschouwer, F., Krachler, M., Debaille, V., Stille, P., Mattielli, N., van der Knaap,
780 W.O., van Leeuwen, J.F.N., Shotyk, W., 2012. Volcano- and climate-driven changes in atmospheric dust
781 sources and fluxes since the Late Glacial in Central Europe. *Geology* 40, 335-338.

782 Letelier, R.M., Björkman, K.M., Church, M.J., Hamilton, D.S., Mahowald, N.M., Scanza, R.A., Schneider, N.,
783 White, A.E., Karl, D.M., 2019. Climate-driven oscillation of phosphorus and iron limitation in the North
784 Pacific Subtropical Gyre. *Proceedings of the National Academy of Sciences* 116, 12720-12728.

785 Li, C., Sonke, J.E., Le Roux, G., Van der Putten, N., Piotrowska, N., Jeandel, C., Mattielli, N., Benoit, M.,
786 Wiggs, G.F.S., De Vleeschouwer, F., 2020. Holocene dynamics of the southern westerly winds over the
787 Indian Ocean inferred from a peat dust deposition record. *Quaternary Science Reviews* 231, 106169.

788 Li, G., Chen, J., Ji, J., Yang, J., Conway, T.M., 2009. Natural and anthropogenic sources of East Asian dust.
789 *Geology* 37, 727-730.

790 Li, G., Wang, Z., Zhao, W., Jin, M., Wang, X., Tao, S., Chen, C., Cao, X., Zhang, Y., Yang, H. and Madsen, D.
791 (2020a) Quantitative precipitation reconstructions from Chagan Nur revealed lag response of East Asian
792 summer monsoon precipitation to summer insolation during the Holocene in arid northern China.
793 *Quaternary Science Reviews* 239, 106365.

794 Li, G., Zhang, H., Liu, X., Yang, H., Wang, X., Zhang, X., Jonell, T.N., Zhang, Y., Huang, X., Wang, Z., Yixuan,
795 W., Yu, L. and Xia, D. (2020b) Paleoclimatic changes and modulation of East Asian summer monsoon by
796 high-latitude forcing over the last 130,000 years as revealed by independently dated loess-paleosol
797 sequences on the NE Tibetan Plateau. *Quaternary Science Reviews* 237, 106283.

798 Li, Q., Wu, H., Guo, Z., Yu, Y., Ge, J., Wu, J., Zhao, D., Sun, A., 2014. Distribution and vegetation
799 reconstruction of the deserts of northern China during the mid-Holocene. *Geophysical Research Letters*
800 41, 5184-5191.

801 Li, Y., Morrill, C., 2015. A Holocene East Asian winter monsoon record at the southern edge of the Gobi
802 Desert and its comparison with a transient simulation. *Climate Dynamics* 45, 1219-1234.

803 Liu, J., Chu, G., Han, J., Rioual, P., Jiao, W., Wang, K., 2009. Volcanic eruptions in the Longgang volcanic
804 field, northeastern China, during the past 15,000 years. *Journal of Asian Earth Sciences* 34, 645-654.

805 Liu, X., Sun, Y., Vandenbergh, J., Cheng, P., Zhang, X., Gowan, E.J., Lohmann, G. and An, Z. (2020)
806 Centennial- to millennial-scale monsoon changes since the last deglaciation linked to solar activities and
807 North Atlantic cooling. *Clim. Past* 16, 315-324.

808 Lu, H., Yi, S., Xu, Z., Zhou, Y., Zeng, L., Zhu, F., Feng, H., Dong, L., Zhuo, H., Yu, K., Mason, J., Wang, X., Chen,
809 Y., Lu, Q., Wu, B., Dong, Z., Qu, J., Wang, X., Guo, Z., 2013. Chinese deserts and sand fields in Last Glacial
810 Maximum and Holocene Optimum. *Chinese Science Bulletin* 58, 2775-2783.

811 Makohonienko, M., Kitagawa, H., Naruse, T., Nasu, H., Momohara, A., Okuno, M., Fujiki, T., Liu, X., Yasuda,
812 Y., Yi, H., 2004. Late-Holocene natural and anthropogenic vegetation changes in the Dongbei Pingyuan
813 (Manchurian Plain), northeastern China. *Quaternary International* 123-125, 71-88.

814 Makohonienko, M., Kitagawa, H., Fujiki, T., Liu, X., Yasuda, Y., Yin, H., 2008. Late Holocene vegetation
815 changes and human impact in the Changbai Mountains area, Northeast China. *Quaternary International*
816 184, 94-108.

817 Marx, S.K., Kamber, B.S., McGowan, H.A., Petherick, L.M., McTainsh, G.H., Stromsoe, N., Hooper, J.N., May,
818 J.-H., 2018. Palaeo-dust records: A window to understanding past environments. *Global and Planetary*
819 *Change* 165, 13-43.

820 Marzin, C., Braconnot, P., Kageyama, M., 2013. Relative impacts of insolation changes, meltwater fluxes
821 and ice sheets on African and Asian monsoons during the Holocene. *Climate Dynamics* 41, 2267-2286.

822 McLennan, S.M., 1989. Rare earth elements in sedimentary rocks; influence of provenance and
823 sedimentary processes. *Reviews in Mineralogy and Geochemistry* 21, 169-200.

824 Meyer, I., Davies, G.R., Stuu, J.-B.W., 2011. Grain size control on Sr-Nd isotope provenance studies and
825 impact on paleoclimate reconstructions: An example from deep-sea sediments offshore NW Africa.
826 *Geochemistry, Geophysics, Geosystems* 12.

827 Miyazaki, T., Kimura, J.-I., Katakuse, M., 2016. Geochemical records from loess deposits in Japan over the
828 last 210 kyr: Lithogenic source changes and paleoclimatic indications. *Geochemistry, Geophysics,*
829 *Geosystems* 17, 2745-2761.

830 Nagashima, K., Tada, R., Tani, A., Toyoda, S., Sun, Y., Isozaki, Y., 2007. Contribution of aeolian dust in Japan
831 Sea sediments estimated from ESR signal intensity and crystallinity of quartz. *Geochemistry, Geophysics,*
832 *Geosystems* 8.

833 Nagashima, K., Tada, R., Toyoda, S., 2013. Westerly jet-East Asian summer monsoon connection during
834 the Holocene. *Geochemistry, Geophysics, Geosystems* 14, 5041-5053.

835 Nakano, T., Yokoo, Y., Nishikawa, M., Koyanagi, H., 2004. Regional Sr-Nd isotopic ratios of soil minerals in
836 northern China as Asian dust fingerprints. *Atmospheric Environment* 38, 3061-3067.

837 Nesbitt, H.W., 1979. Mobility and fractionation of rare earth elements during weathering of a granodiorite.
838 *Nature* 279, 206.

839 Peng, Z.C., Zartman, R.E., Futa, K., Chen, D.G., 1986. Pb-, Sr- and Nd-isotopic systematics and chemical
840 characteristics of Cenozoic basalts, eastern China. *Chemical Geology: Isotope Geoscience section* 59, 3-33.

841 Pratte, S., Bao, K., Sapkota, A., Zhang, W., Shen, J., Le Roux, G., De Vleeschouwer, F., 2020. 14 kyr of
842 atmospheric mineral dust deposition in north-eastern China: A record of palaeoclimatic and
843 palaeoenvironmental changes in the Chinese dust source regions. *The Holocene* 30, 492-506.

844 Pratte, S., Garneau, M., De Vleeschouwer, F., 2017. Late-Holocene atmospheric dust deposition in eastern
845 Canada (St. Lawrence North Shore). *The Holocene* 27, 12-25.

846 Rao, W., Chen, J.U.N., Yang, J., Ji, J., Li, G., Tan, H., 2008. Sr-Nd isotopic characteristics of eolian deposits
847 in the Erdos Desert and Chinese Loess Plateau: Implications for their provenances. *Geochemical Journal*
848 42, 273-282.

849 Rao, W., Tan, H., Jiang, S., Chen, J., 2011. Trace element and REE geochemistry of fine- and coarse-grained
850 sands in the Ordos deserts and links with sediments in surrounding areas. *Geochemistry* 71, 155-170.

851 Roe, G., 2009. On the interpretation of Chinese loess as a paleoclimate indicator. *Quaternary Research* 71,
852 150-161.

853 Schettler, G., Liu, Q., Mingram, J., Negendank, J.F.W., 2006a. Palaeovariations in the East-Asian Monsoon
854 Regime Geochemically Recorded in Varved Sediments of Lake Sihailongwan (Northeast China, Jilin
855 Province). Part 1: Hydrological Conditions and Dust Flux. *Journal of Paleolimnology* 35, 239-270.

856 Schettler, G., Mingram, J., Negendank, J.F.W., Jiaqi, L., 2006b. Palaeovariations in the East-Asian Monsoon
857 Regime Geochemically Recorded in Varved Sediments of Lake Sihailongwan (Northeast China, Jilin

858 Province). Part 2: a 200-Year Record of Atmospheric Lead-210 Flux Variations and its Palaeoclimatic
859 Implications. *Journal of Paleolimnology* 35, 271-288.

860 Schiemann, R., Lüthi, D., Schär, C., 2009. Seasonality and Interannual Variability of the Westerly Jet in the
861 Tibetan Plateau Region. *Journal of Climate* 22, 2940-2957.

862 Sharifi, A., Murphy, L.N., Pourmand, A., Clement, A.C., Canuel, E.A., Naderi Beni, A., A.K. Lahijani, H.,
863 Delanghe, D., Ahmady-Birgani, H., 2018. Early-Holocene greening of the Afro-Asian dust belt changed
864 sources of mineral dust in West Asia. *Earth Planet Sc Lett* 481, 30-40.

865 Sharifi, A., Pourmand, A., Canuel, E.A., Ferer-Tyler, E., Peterson, L.C., Aichner, B., Feakins, S.J., Daryaee, T.,
866 Djamali, M., Beni, A.N., Lahijani, H.A.K., Swart, P.K., 2015. Abrupt climate variability since the last
867 deglaciation based on a high-resolution, multi-proxy peat record from NW Iran: The hand that rocked the
868 Cradle of Civilization? *Quaternary Science Reviews* 123, 215-230.

869 Shi, P., Song, C., 2003. Palynological records of environmental changes in the middle part of Inner
870 Mongolia, China. *Chinese Science Bulletin* 48, 1433-1438.

871 Shotyk, W., 1997. Atmospheric deposition and mass balance of major and trace elements in two oceanic
872 peat profiles, northern Scotland and Shetland Islands. *Chemical Geology* 138, 55-72.

873 Song, Q., 1987a. Chinese Population: Inner Mongolia Branch. China Financial and Economic Publishing
874 House. (in Chinese)

875 Song, Q., 1987b. Chinese Population: Jilin Branch. China Financial and Economic Publishing House. (in
876 Chinese)

877 Steinmann, P., Shotyk, W., 1997. Geochemistry, mineralogy, and geochemical mass balance on major
878 elements in two peat bog profiles (Jura Mountains, Switzerland). *Chemical Geology* 138, 25-53.

879 Stevens, T., Marković, S.B., Zech, M., Hambach, U. and Sümegi, P. (2011) Dust deposition and climate in
880 the Carpathian Basin over an independently dated last glacial–interglacial cycle. *Quaternary Science*
881 *Reviews* 30, 662-681.

882 Sun, D., Bloemendal, J., Rea, D.K., An, Z., Vandenberghe, J., Lu, H., Su, R. and Liu, T. (2004) Bimodal grain-
883 size distribution of Chinese loess, and its palaeoclimatic implications. *CATENA* 55, 325-340.

884 Sun, J., Zhang, M., Liu, T., 2001. Spatial and temporal characteristics of dust storms in China and its
885 surrounding regions, 1960–1999: Relations to source area and climate. *Journal of Geophysical Research:*
886 *Atmospheres* 106, 10325-10333.

887 Taylor, S.R., McLennan, S.M., 1985. The continental crust: Its composition and evolution. Blackwell
888 Scientific, Oxford.

889 Taylor, W., 2000. Change-point analysis: A powerful new tool for detecting changes. Retrieved from:
890 <http://www.variation.com/cpa/techchangept.html>

891 Tsoar, H., Pye, K., 1987. Dust transport and the question of desert loess formation. *Sedimentology* 34,
892 139-153.

893 Vanneste, H., De Vleeschouwer, F., Martínez-Cortizas, A., von Scheffer, C., Piotrowska, N., Coronato, A.,
894 Le Roux, G., 2015. Late-glacial elevated dust deposition linked to westerly wind shifts in southern South
895 America. *Scientific Reports* 5.

896 Wang, H., Chen, J., Zhang, X., Chen, F., 2014. Palaeosol development in the Chinese Loess Plateau as an
897 indicator of the strength of the East Asian summer monsoon: Evidence for a mid-Holocene maximum.
898 *Quaternary International* 334-335, 155-164.

899 Wang, K., Tada, R., Zheng, H., Irino, T., Zhou, B., Saito, K., 2020. Provenance changes in fine detrital quartz
900 in the inner shelf sediments of the East China Sea associated with shifts in the East Asian summer monsoon
901 front during the last 6 kyrs. *Progress in Earth and Planetary Science* 7, 5.

902 Wang, L., Li, J., Lu, H., Gu, Z., Rioual, P., Hao, Q., Mackay, A.W., Jiang, W., Cai, B., Xu, B., Han, J., Chu, G.,
903 2012. The East Asian winter monsoon over the last 15,000 years: its links to high-latitudes and tropical
904 climate systems and complex correlation to the summer monsoon. *Quaternary Science Reviews* 32, 131-
905 142.

906 Wedepohl, K.H., 1995. The composition of the continental crust. *Geochimica et Cosmochimica Acta* 59,
907 1217-1232.

908 Wen, R., Xiao, J., Chang, Z., Zhai, D., Xu, Q., Li, Y., Itoh, S., 2010. Holocene precipitation and temperature
909 variations in the East Asian monsoonal margin from pollen data from Hulun Lake in northeastern Inner
910 Mongolia, China. *Boreas* 39, 262-272.

911 Wen, R., Xiao, J., Fan, J., Zhang, S., Yamagata, H., 2017. Pollen evidence for a mid-Holocene East Asian
912 summer monsoon maximum in northern China. *Quaternary Science Reviews* 176, 29-35.

913 Wilson, M., 2000. *Igneous Petrogenesis: A Global Tectonic Approach*. Kluwer Academic Publishers, London

914 Xia, D., Jia, J., Li, G., Zhao, S., Wei, H. and Chen, F. (2014) Out-of-phase evolution between summer and
915 winter East Asian monsoons during the Holocene as recorded by Chinese loess deposits. *Quaternary*
916 *Research* 81, 500-507.

917 Xie, Y., Chi, Y., 2016. Geochemical investigation of dry- and wet-deposited dust during the same dust-
918 storm event in Harbin, China: Constraint on provenance and implications for formation of aeolian loess.
919 *Journal of Asian Earth Sciences* 120, 43-61.

920 Xie, Y., Kang, C., Chi, Y., Du, H., Wang, J., Sun, L., 2019. The loess deposits in Northeast China: The linkage
921 of loess accumulation and geomorphic-climatic features at the easternmost edge of the Eurasian loess
922 belt. *Journal of Asian Earth Sciences* 181, 103914.

923 Xie, Y., Liu, L., Kang, C., Chi, Y., 2020. Sr-Nd isotopic characteristics of the Northeast Sandy Land, China and
924 their implications for tracing sources of regional dust. *Catena* 184, 104303.

925 Xie, Y., Yuan, F., Zhan, T., Kang, C., Chi, Y., Ma, Y., 2017. Geochemistry of loess deposits in northeastern
926 China: constraint on provenance and implication for disappearance of the large Songliao palaeolake.
927 *Journal of the Geological Society* 175, 146-162.

928 Xu, B., Wang, L., Gu, Z., Hao, Q., Wang, H., Chu, G., Jiang, D., Liu, Q., Qin, X., 2018. Decoupling of Climatic
929 Drying and Asian Dust Export During the Holocene. *Journal of Geophysical Research: Atmospheres* 123,
930 915-928.

931 Xu, Z., Mason, J.A., Xu, C., Yi, S., Bathiany, S., Yizhaq, H., Zhou, Y., Cheng, J., Holmgren, M., Lu, H., 2020.
932 Critical transitions in Chinese dunes during the past 12,000 years. *Science Advances* 6, eaay8020.

933 Yan, J., Zhao, J.X., Liu, H.Q., 2007. Quaternary basalts from Longgang in the North China Craton:
934 petrogenesis and characteristics of the mantle source. *Acta Petrologica Sinica* 23, 1413-1422. (in Chinese)

935 Yang, J., Li, G., Rao, W., Ji, J., 2009. Isotopic evidences for provenance of East Asian Dust. *Atmospheric*
936 *Environment* 43, 4481-4490.

937 Yang, S. and Ding, Z. (2008) Advance–retreat history of the East-Asian summer monsoon rainfall belt over
938 northern China during the last two glacial–interglacial cycles. *Earth Planet Sc Lett* 274, 499-510.

939 Yang, S. and Ding, Z. (2014) A 249 kyr stack of eight loess grain size records from northern China
940 documenting millennial-scale climate variability. *Geochemistry, Geophysics, Geosystems* 15, 798-814.

941 Yang, X., Liang, P., Zhang, D., Li, H., Rioual, P., Wang, X., Xu, B., Ma, Z., Liu, Q., Ren, X., Hu, F., He, Y., Rao,
942 G., Chen, N., 2019. Holocene aeolian stratigraphic sequences in the eastern portion of the desert belt
943 (sand seas and sandy lands) in northern China and their palaeoenvironmental implications. *Science China*
944 *Earth Sciences* 62, 1302-1315.

945 Zaarur, S., Stein, M., Adam, O., Mingram, J., Liu, J., Wu, J., Raveh-Rubin, S., Erel, Y., 2020. Synoptic stability
946 and anomalies in NE China inferred from dust provenance of Sihailongwan maar sediments during the
947 past ~80 kyr. *Quaternary Science Reviews* 239, 106279.

948 Zeng, L., Yi, S., Zhang, W., Feng, H., Lv, A., Zhao, W., Luo, Y., Wang, Q., Lu, H., 2020. Provenance of loess
949 deposits and stepwise expansion of the desert environment in NE China since ~1.2 Ma: Evidence from Nd-
950 Sr isotopic composition and grain-size record. *Global and Planetary Change* 185, 103087.

951 Zhang, K., Gao, H., 2007. The characteristics of Asian-dust storms during 2000–2002: From the source to
952 the sea. *Atmospheric Environment* 41, 9136-9145.

953 Zhang, M., Bu, Z., Jiang, M., Wang, S., Liu, S., Chen, X., Hao, J., Liao, W., 2019. The development of Hani
954 peatland in the Changbai mountains (NE China) and its response to the variations of the East Asian
955 summer monsoon. *Science of The Total Environment* 692, 818-832.

956 Zhang, W., Chen, J., Ji, J., Li, G., 2016. Evolving flux of Asian dust in the North Pacific Ocean since the late
957 Oligocene. *Aeolian Research* 23, 11-20.

958 Zhang, W., Hou, S., Liu, Y., Wu, S., An, W., Pang, H., Wang, C., 2017. A high-resolution atmospheric dust
959 record for 1810–2004 A.D. derived from an ice core in eastern Tien Shan, central Asia. *Journal of*
960 *Geophysical Research: Atmospheres* 122, 7505-7518.

961 Zhang, W., Zhang, E., Liu, E., Abell, J.T., Sun, W., Ni, Z., Chen, R., Cai, Y., Meng, X., 2023. Mongolian dust
962 activity over the last 25 kyr predominantly driven by the East Asian winter monsoon: insights from the
963 geochemistry of lake Tuofengling sediments. *Geophysical Research Letters* 50, e2023GL103633.

964 Zhang, W., Zhao, J.-x., Chen, J., Ji, J., Liu, L., 2018a. Binary sources of Chinese loess as revealed by trace
965 and REE element ratios. *Journal of Asian Earth Sciences* 166, 80-88.

966 Zhang, X., Jin, L., Lu, H., Park, W., Schneider, B., Latif, M., 2018b. East-west contrast of Northeast Asian
967 summer precipitation during the Holocene. *Global and Planetary Change* 170, 190-200.

968 Zhao, H., Liu, J., Hall, V.A., Li, X., 2017. Tephrostratigraphical investigation of lake sediments and a peat
969 bog in Northeastern China since 20,000 years. *The Holocene* 27, 765-778.

970 Zhao, W., Sun, Y., Balsam, W., Zeng, L., Lu, H., Otgonbayar, K., Ji, J., 2015. Clay-sized Hf-Nd-Sr isotopic
971 composition of Mongolian dust as a fingerprint for regional to hemispherical transport. *Geophysical*
972 *Research Letters* 42, 5661-5669.

973 Zhao, W., Xie, S., 1988. Human population in China. People's Publishing House, Beijing. (in Chinese)

974 Zhong, H., Li, D., 2005. Relationship between sand dust storm in northern China in April and Westerly
975 Circulation. *Plateau Meteorology* 24, 104–111. (in Chinese)

976 Zhou, P., Shi, Z., Li, X., Zhou, W., 2020. Response of Westerly Jet over the Northern Hemisphere to
977 astronomical insolation during the Holocene. *Frontiers in Earth Science* 8.

978 Zhou, X., Sun, L., Zhan, T., Huang, W., Zhou, X., Hao, Q., Wang, Y., He, X., Zhao, C., Zhang, J., Qiao, Y., Ge,
979 J., Yan, P., Yan, Q., Shao, D., Chu, Z., Yang, W., Smol, J.P., 2016. Time-transgressive onset of the Holocene
980 Optimum in the East Asian monsoon region. *Earth Planet Sc Lett* 456, 39-46.

981 Zhou, X., Zhan, T., Tan, N., Tu, L., Smol, J.P., Jiang, S., Zeng, F., Liu, X., Li, X., Liu, G., Liu, Y., Zhang, R., Shen,
982 Y., 2023. Inconsistent patterns of Holocene rainfall changes at the East Asian monsoon margin compared
983 to the core monsoon region. *Quaternary Science Reviews* 301, 107952.

984

985

986